Optical Materials 157 (2024) 116068

Contents lists available at ScienceDirect

Optical Materials

journal homepage: www.elsevier.com/locate/optmat

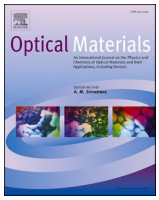

Research Article

Optical limiting and third-order nonlinear optical properties of thiazole-based chalcone derivative: Insights from experimental and theoretical approaches

Keerthikumara Venkatesha [a], Mahesh Sankanahalli Srinivas [b], Ananda Swamynayaka [a], Mahendra Madegowda [a,*], Ravi Singh Krishna [c], Tejaswi Ashok Hegde [d], Maralinganadoddi P. Sadashiva [c]

[a] Department of Studies in Physics, Manasagangotri, University of Mysore, Mysuru, 570 006, Karnataka, India
[b] Acharya Institute of Technology, Soladevanahalli, Bangalore, 560 107, India
[c] Department of Studies in Chemistry, Manasagangotri, University of Mysore, Mysuru, 570 006, Karnataka, India
[d] Department of Physics, Hindustan Institute of Technology and Science, Chennai, 603 103, India

ARTICLE INFO

Keywords:
NLO
Thiazole derivative
DFT
Z-Scan technique
Optical limiting
first and second hyperpolarizability

ABSTRACT

The current study delves into exploring the linear and nonlinear optical properties of (E)-3-(4-methylthiazole-5-yl)-1-(3-nitrophenyl)prop-2-en-1-one (MNP) through a combined approach of theoretical predictions and experimental observations. By employing single crystal X-ray diffraction analysis, the MNP's crystal structure has been confirmed, establishing its categorization as triclinic with the *P*-1 space group. The grown crystal was characterized through UV–Vis studies, photoluminescence studies, and thermal analysis. The absorption spectrum of MNP was examined using UV–Vis analysis in various solvents, revealing a strong absorption peak between 335 and 357 nm, suggesting its suitability for UV-based optoelectronic applications also the MNP exhibits good nonlinear optical (NLO) responses, including α_{CT}, β_{CT}, and γ_{CT} values, across different solvent environments. The examination of MNP's third-order nonlinear optical properties and its optical limiting behavior was conducted using the Z-scan technique with a continuous wave (CW) laser at 532 nm. The results revealed substantial $\chi^{(3)}$ values of 3.01×10^{-6} esu, and an optical limiting threshold observed at 4.213×10^{3} Wcm^{-2}. The experimental results were corroborated by theoretical calculations derived from density functional theory (DFT). DFT calculations were used to explore MNP's electronic structure and charge distribution, utilizing FMO, MEP, and NBO analysis. Furthermore, the time-dependent Hartree-Fock (TDHF) method was employed to compute the static and dynamic linear polarizability (α) along with the first and second hyperpolarizability (β and γ) of MNP. Notably, the first hyperpolarizability exceeded the urea standard by 91.03 times at a wavelength of 532 nm, and the computed second-order hyperpolarizability value of 0.42×10^{-32}esu. closely matches the experimental observations in DMSO solvent (0.25×10^{-31}esu). Overall, the findings of these studies indicate that the synthesized chalcone derivative material holds potential for optoelectronic applications.

1. Introduction

At the forefront era of contemporary materials science, researchers are deeply engaged in exploring nonlinear optical (NLO) materials, with due recognition as pivotal in advancing various technological domains, including signal processing, optical communication, and laser systems [1]. In recent years, we have witnessed a surge in interest in organic materials, attributed to their distinctive molecular structures and electronic properties. Among the various organic materials, chalcone derivatives, distinguished by their heterocyclic aromatic ring, have garnered attention for their potential in both NLO applications and pharmaceutical industries [2–5]. As a part of our continuous interest in looking for the different organic functional as hybrid component inclusion in the primary chalcones [6–8], we have made an intricate design with an organic substituted heterocyclic thiazole ring as a π-conjugated linker in the current chalcone material. The importance of

* Corresponding author. DOS in Physics, Manasagangotri, University of Mysore, Mysuru, 570006, Karnataka, India.
E-mail address: mahendra@physics.uni-mysore.ac.in (M. Madegowda).

https://doi.org/10.1016/j.optmat.2024.116068
Received 22 April 2024; Received in revised form 5 August 2024; Accepted 3 September 2024
Available online 15 September 2024

such thiazole as a motif holds a pivotal position in drug design in the pharmaceutical field, which owes due to its wide range of biological activities, such as antifungal [9], anti-allergic [10], antihypertensive [11], antiviral [12], antioxidant [13], antibacterial [14], anti-schizophrenia [15], and anticancer [16] properties. Notably, thiazole is a key pharmacophore utilized in cancer therapy by drugs such as, meloxicam [17], fanetizole [18], ritonavir [19–21], bleomycin [21], and sulfathiazole [22]. Moreover, hydrazinyl thiazole, a derivative of thiazole, demonstrates substantial biological effects, encompassing antimalarial [23], antioxidant [24], antitumor [25], and antifungal [26] activities.

Beyond their importance in biological applications, chalcone scaffolds with thiazole motifs have garnered considerable attention in the field of NLO, drawing significant interest from both theoretical and experimental researchers [5,27]. The properties of thiazole, such as its ultrafast broadband electrical responsiveness and low dielectric constants, are the driving force behind this renewed interest. These exceptional properties have garnered increased attention due to their potential to lead to significant advancements in cutting-edge optoelectronic technologies [28,29]. Recently, there have been reports of synthesis and investigation of chromophores that feature a π-conjugated five-membered heterocycle, like thiazole, pyrrole, and thiophene, as the donor component, and a heterocyclic ring, such as pyrazine, pyridazine, and pyrimidine, as the acceptor group [30]. These chromophores have displayed a variety of properties, including solvatochromic, fluorescence, photochromic, and NLO characteristics [31–33]. In the literature, Raposo et al. [34] designed and synthesized a sequence of π-conjugated systems with donor-acceptor substitution, utilizing 1-alkyl (aryl) thienylpyrroles as donor units and functionalizing them with various acceptor groups, including benzothiazolyl, dicyanovinyl, thiazolyldiazene, benzimidazolyl, and aryldiazene. Their study delved into the materials' electrochemical and optical behaviors, both linear and nonlinear, unveiling their substantial potential for second-order NLO and photochromic applications [35,36]. Naveena et al. [37] synthesized a series of thiazole-based compounds. In this article, they highlight the nonlinear optical (NLO) properties, optoelectronic materials, and their potential applications in cutting-edge technologies. In parallel, thiazole derivatives have emerged as noteworthy subjects of study, particularly those featuring unsymmetrical thiazole rings and extended π-conjugated systems [38]. These compounds have been observed to display significant values in second harmonic generation [39,40], forming a promising cornerstone for optoelectronic endeavors in both technology and industrial domains. Several experimental and theoretical investigations have demonstrated that substituting the benzene ring in a chromophore bridge with easily delocalizable heterocycles, such as pyrole, thiazole, thiophene, and imidazole, increases molecular hyperpolarizability in the resulting push-pull systems [41]. Moreover, experimental and theoretical investigations have underscored the critical role of the thiazole ring in NLO materials, elucidating its influence on parameters such as asymmetric polarization, conformational linearity, conjugate length, intermolecular charge transfer (ICT), and the positioning of donor and acceptor groups, all of which significantly impact nonlinear optical characteristics [42,43].

Acknowledging the significance of the aforementioned strategies, employed in the selection of NLO-responsive molecule, we designed, synthesized, and characterized a newly synthesized chalcone derivative, (E)-3-(4-methylthiazole-5-yl)-1-(3-nitrophenyl)prop-2-en-1-one (MNP). The compound is characterized using various techniques, namely SC-XRD, NMR (^{13}C and ^{1}H), FT-IR, UV–Vis–NIR, photoluminescence, solvatochromic studies, and TG-DTA. These investigations focus on understanding the compound's structural, spectroscopic attributes and thermal behaviors. The Z-scan method is employed to analyze the third-order NLO characteristics. The amalgamation of experimental methods and DFT simulations facilitates a comprehensive exploration of the NLO characteristics of the MNP compound. Overall, the study aims to develop and characterize new organic chalcone material with potent NLO properties, particularly thiazole-linked systems, for potential use in diverse optoelectronic technologies.

2. Materials and methods

2.1. Material synthesis and crystal growth

A new chalcone derivative, (E)-3-(4-methylthiazole-5-yl)-1-(3-nitrophenyl)prop-2-en-1-one (MNP), was prepared through the Claisen-Schmidt condensation technique. In a round-bottom flask, 3-nitro acetophenone (0.01 mol) (**1**) and 4-methylthiazole-5-carboxaldehyde (0.01 mol) (**2**) were combined in a 1:1 ratio in an ethanol solvent. Subsequently, 10 ml of sodium hydroxide (NaOH) was introduced into the mixture and agitated for 5 hours in an ice-cold bath. The progress of the reaction and the compound's purity were monitored using thin-layer chromatography (TLC). On completion of the reaction, the resultant compound was introduced into ice-cold water containing 2 ml of hydrochloric acid (HCl) and was allowed to settle and precipitate for 5 hours. The resultant product was obtained through filtration and then subjected to air drying at room temperature for 24 hours. The obtained crude product upon crystallization using ethyl acetate solvent, a good-quality transparent pale yellowish color crystals obtained after 25 days with the dimensions 0.150 × 0.181 × 0.344 (mm)^3. Fig. 1 depicts the single crystal of grown MNP. The synthesis pathway of MNP (**3**) is illustrated in Scheme 1, and its spectroscopic data (^{1}H and ^{13}C NMR) are provided in the supporting information.

2.2. Experimental details

Single crystal XRD data for the MNP were acquired at standard room temperature (293 K) employing a Bruker AXS kappa Apex2 CCD Diffractometer with graphite monochromatic MoKα radiation (λ = 0.71073). The NMR spectra of the MNP compound, encompassing both ^{13}C and ^{1}H, were scrutinized using deuterated chloroform ($CDCl_3$) as the solvent. This analysis was conducted utilizing an Agilent 600 MR DD2 NMR spectrometer. The FTIR spectrum of the MNP sample was obtained at ambient temperature using a 'PerkinElmer Spectrum Two' spectrophotometer. The analysis was conducted through the solution method across the range of 4000-400 cm^{-1} for the identification of functional groups and to assess the formation of crystalline materials. The MNP's optical transmittance and solvatochromic spectrum were examined within the 270–500 nm range using various solvents with a "Beckman Coulter-DU 73″ UV–visible spectrophotometer. The F-7000-FL spectrophotometer was utilized to record the photoluminescence (PL) spectrum within the range from 375 to 750 nm. The MNP's thermal properties were studied using the TGA/DTA technique, with the NETZSCH STA 2500 instrument under a dry nitrogen (N_2) atmosphere. The analysis was conducted from 30°C to 1400°C with a heating rate set at 20°C/min. The third-order NLO studies of the studied compound (i.e., MNP) were conducted using the Z-scan technique with the HOLMARC Z-scan Model: HOEDLOE-03 to determine NLO parameters such as nonlinear optical susceptibility ($\chi^{(3)}$), nonlinear refractive index (n_2), and nonlinear absorption coefficient (β).

2.3. Computational details

The MNP compound's quantum chemical calculations were executed with Gaussian 09 software [44]. The molecular structure was optimized through DFT at the B3LYP level, utilizing a 6–311++G(d,p) basis set. The resulting optimized structure was visualized using GaussView6 [44]. The vibrational wavenumber was computed at the same level of theory, and no imaginary frequencies were detected in the optimized MNP structure. All the computed wavenumbers were interpreted through the PED approach using the VEDA program [45]. The HOMO-LUMO levels and Natural Bond Orbitals (NBO) analysis were performed at the B3LYP/6–311++G(d,p) level to explain the

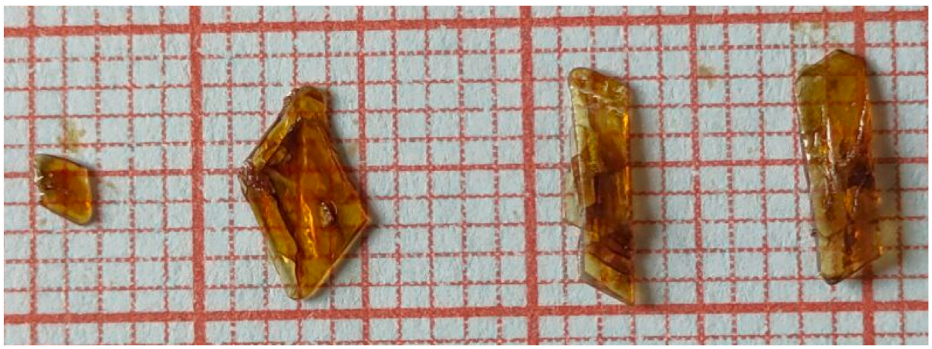

Fig. 1. Photograph of grown MNP single crystal.

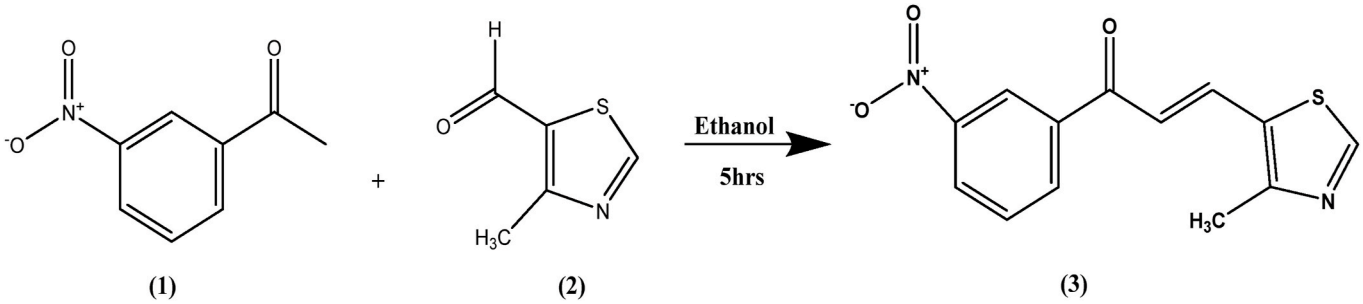

Scheme 1. Synthesis pathway of MNP.

intermolecular charge transfer within the molecule. The electrophilic and nucleophilic regions of the molecule were determined through MEP analysis. Furthermore, the NLO properties, including dipole moment (μ), linear polarizabilities (α), and first and second hyperpolarizabilities (β and γ), were calculated at various frequencies (i.e., different wavelengths) using the HF/6-31G(d,p) basis set via the GAMESS software [46]. Total dipole moment (μ), the static and dynamic values of <α>, Δα, <β>, and <γ>^{THG} were calculated by the following relations.

$$\mu = \left(\mu_x^2 + \mu_y^2 + \mu_z^2\right)^{1/2} \quad (1)$$

$$< \alpha > = \frac{1}{3}\left(\alpha_{xx} + \alpha_{yy} + \alpha_{zz}\right) \quad (2)$$

$$\Delta\alpha = \frac{1}{\sqrt{2}}\left[\left(\alpha_{xx} + \alpha_{yy}\right)^2 + \left(\alpha_{yy} + \alpha_{zz}\right)^2 + \left(\alpha_{zz} + \alpha_{xx}\right)^2 + 6\left(\alpha_{xy}^2 + \alpha_{xz}^2 + \alpha_{yz}^2\right)\right]^{1/2} \quad (3)$$

$$< \beta > = \left[\left(\beta_{xxx} + \beta_{yyy} + \beta_{zzz}\right)^2 + \left(\beta_{yyy} + \beta_{yzz} + \beta_{yxx}\right)^2 + \left(\beta_{zzz} + \beta_{zxx} + \beta_{zyy}\right)^2\right]^{1/2} \quad (4)$$

$$< \gamma >^{THG} = \frac{1}{5}\left[\left(\gamma_{xxxx} + \gamma_{yyyy} + \gamma_{zzzz}\right) + 2\left(\gamma_{xxyy} + \gamma_{xxzz} + \gamma_{yyzz}\right)\right] \quad (5)$$

The conversion factors were applied to transform tensor components from a.u. to e.s.u. The factor for α is 1 a.u. = 0.15×10^{-24} esu, for β 1a.u. = 8.64×10^{-33} esu, and for γ 1a.u. = 5.04×10^{-40} esu.

3. Results and discussion

3.1. Crystal structure description

A new pale-yellow crystal measuring $0.150\times0.181\times0.344$ (mm)^3 was chosen for crystallographic examination. It was delicately positioned on the goniometer of the Bruker Kappa APEX II single-crystal XRD. The selected crystal underwent diffraction analysis at 293 K, using a precisely calibrated monochromatic graphite-sealed tube, covering the angular range from 2.80° to 29.63° ($2.80° \leq \theta \leq 29.63°$). The crystal structure was determined using the direct method with the SHELXS 18 program and subsequently refined using the SHELXL 18 [47] program through full-matrix least squares on F^2. The refinement process involved 173 parameters and utilized 3555 distinct reflections, resulting in a convergence with R = 0.0473 (wR = 0.1309) and a goodness-of-fit

Table 1
Crystal data and structure refinement details of MNP.

Empirical formula	C_{13} H_{10} N_2 O_3 S
Formula weight	274.29
Temperature	298
Wavelength	0.71073 Å
Reflns. for cell determination	9996
θ range for the above	2.94°–29.59°
Crystal system	triclinic
Space group	*P*-1
Cell dimensions	a = 7.7861 (9) Å, b = 8.2117 (9) Å, c = 11.1908 (11) Å α = 81.436 (4)°, β = 84.720 (4)° γ = 63.052 (4)°
Volume	630.46 (12) Å^3
Z	2
Density (calculated)	1.445 Mg m^{-3}
Absorption coefficient	0.262 mm^{-1}
F_{000}	284
Crystal size	0.150 mm × 0.181 mm × 0.344 mm
θ range for data collection	2.80°–29.63°
Index ranges	$-10 \leq h \leq 10$ $-11 \leq k \leq 11$ $-15 \leq l \leq 15$
Reflections collected	32509
Independent reflections	3555
Refinement method	full-matrix least-squares on F^2
Data/restraints/parameters	3543/0/173
Goodness-of-fit on F^2	1.066
Final R indices [$I > 2\sigma(I)$]	$R1$ = 0.0473, w$R2$ = 0.1309
R indices (all data)	$R1$ = 0.0570, w$R2$ = 0.1411
Largest diff. peak and hole	0.438; −0.192 e Å^{-3}

on F^2 of 1.066. Thermal ellipsoidal plots were generated using Mercury 4.0 [48], and PLATON [49] was employed for geometrical calculations. Table 1 presents a comprehensive overview of the crystallographic data, measurement details, and refinement parameters. Meanwhile, Fig. 2 depicts the ORTEP representation of the MNP compound, rendered at a 50 % probability level.

The MNP compound exhibits a triclinic crystalline structure, as determined by single crystal XRD analysis, and belongs to the *P*-1 space group, with two molecules in each unit cell. The cell parameters are: a = 7.7861 (9) Å, b = 8.2117 (9) Å, c = 11.1908 (11) Å, α = 81.436 (4)°, β = 84.720 (4)°, γ = 63.052 (4)°, providing essential structural details about the compound's arrangement. The MNP structure was formed by methyl-thiazole (C1–C2–N3–C4–S5–C6) and nitrobenzene (N17 and C11–C16) joined by acrylaldehyde, which acts as a bridge. The entire molecule lies almost planar conformation, with a dihedral angle of nearly 4° between the methyl-thiazole and nitrobenzene fragments. The atoms C1 and C14 display the maximum deviation with of 0.008 Å and 0.181 Å from the methyl-thiazole and nitrobenzene respectively. The carbon atoms (C11–C12–C13–C14–C15–C16) from nitrobenzene ring and (C2–C4–C6) from thiazole ring of the compound exhibit sp2 hybridization. The bond angle values of C14–C15–C16 (123.02°), and C16–C11–C12 (118.95°) of the nitrobenzene ring indicate almost planar trigonal geometry. The nitro groups (O18–N17–O19) attached to the benzene ring show a bent geometry, with a bond angle of 124.7°. Additionally, the torsion angle values O18–N17–C15–C14 (158.6) and O19–N17–C15–C16 (155.1) indicate that the ring adopts an + anti-periplanar conformation.

The optimization of the MNP molecule's geometry was carried out utilizing the B3LYP method in conjunction with the 6–311++G(d,p) basis set, and the resulting optimized structure is illustrated in Fig. 3. While the optimized parameters, such as bond lengths and bond angles, closely match with experimental findings, minor discrepancies are observed in bonds such as C–C, O–N, N–C, and S–C bonds (see Table S1). The carbon-carbon (C–C) bond length in the phenyl ring is about 1.398 Å [50]. In our DFT analysis, C–C bond lengths in the same rings ranged from 1.388 Å to 1.404 Å, closely matching with experimental values (1.378 Å to 1.400 Å), and these results are also seen in the reported compound [51]. Table S1 provides the selected bond lengths, bond angles, and torsion angles for the MNP molecule. It is emphasized that, the differences between the experimentally observed bond lengths and DFT bond lengths should not exceed 0.03 Å while bond angles should not exceed 0.96°.

The crystal structure analysis revealed the presence of significant C–H···O and C–H···N intermolecular interactions, along with C–H···O and C–H···S intramolecular interactions. The intermolecular interactions involving C1–H1···N3 lead to the formation of an eight-membered ring, characterized by a graph set motif of R_2^2 (8) (See Fig. 4b). Detailed information about hydrogen bond interaction is provided in Table 2. In the crystal structure, hydrogen bonds are formed through attractive forces between electronegative atoms and hydrogen atoms. In supramolecular analysis, the molecule's C12 and H12 atoms serve as donors, and N3 and O18 atoms as acceptors. Importantly, weak interactions occur between oxygen atoms of the nitro group with hydrogen atoms. These interactions significantly contribute to the molecule's nonlinear optical effect [52]. Further, the title structure stabilizes by Y-X … Cg1 and face-to-face (Cg1-Cg2/Cg2-Cg1) interaction. Here, Cg1 and Cg2 represent the centroids of two distinct rings: C2–N3–C4–S5–C6 (i.e., thiazole ring) and C11–C12–C13–C14–C15–C16 (i.e., phenyl ring). The Cg1-Cg2/Cg2-Cg1 distance found between the thiazole ring and phenyl ring is 3.675 Å with symmetry operation: 2-X, 1-Y, 1-Z. Additionally, the molecule has N17–O18 … π (Cg1) interaction with a distance of 3.365 Å (symmetry operation: 2-X, -Y, 1-Z). The hydrogen bond interactions, as viewed along the a-axis and centroid-centroid interactions, are illustrated in Fig. 4a.

3.2. FTIR analysis

The molecule's optimized geometry was subjected to vibrational analysis in the gaseous phase. Fig. 5 illustrates the MNP compound's experimental and simulated FT-IR spectra, while Table 3 outlines the chosen vibrational assignments. The theoretical wave numbers below 1700 cm^{-1} are scaled by a factor of 0.983, and those above 1700 cm^{-1} are scaled by 0.958 to enhance their alignment with the experimental and simulated data [53]. Vibrational assignments with a PED greater than 10 % are listed in Table 3. Chalcones are formed by linking two aromatic rings via carbonyl groups, while aliphatic ketones exhibit C=O stretching vibrations between 1730 and 1800 cm^{-1} [54]. The chalcone derivative exhibited carbonyl (C=O) stretching vibrations, exhibited a computed peak at 1682 cm^{-1} with an 88 % PED contribution, while experimentally observed at 1800 cm^{-1}. Typically, in aromatic compounds, C–H stretching vibrations are manifest around 3100-3000 cm^{-1} [54]. In the FT-IR spectra, Compound MNP exhibited a distinct C–H stretching signal for the methylthiazol group at 3094 cm^{-1}, consistent with the computed values of 3017 cm^{-1} with 82 % PED. The observed stretching modes for C–C are recorded at 1657 and 1532 cm^{-1}, while the associated DFT values are at 1589 and 1489 cm^{-1}, respectively [54]. Balachandran et al. [55] identified computed stretching vibrations of the C–S mode at 750 cm^{-1}, which closely matched the DFT value of 805 cm^{-1}. The thiazole (C=N) bond's stretching vibration was experimentally noticed at 1657 cm^{-1}, whereas the calculated value was found to be 1589 cm^{-1}.

In-plane bending C–H vibrations, typically manifest in the range of 1300-1000 cm^{-1}, exhibiting a variety of intensities ranging from strong to weak [56]. In our MNP molecule, the computed bending vibrations of

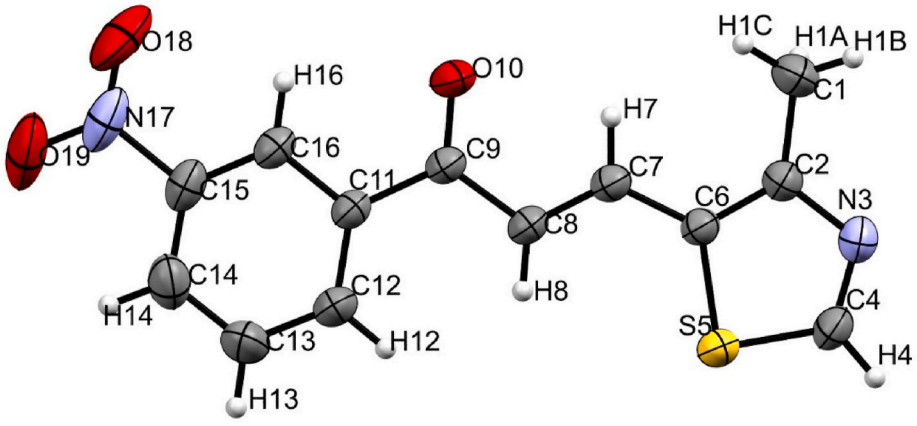

Fig. 2. ORTEP diagram at 50 % probability level.

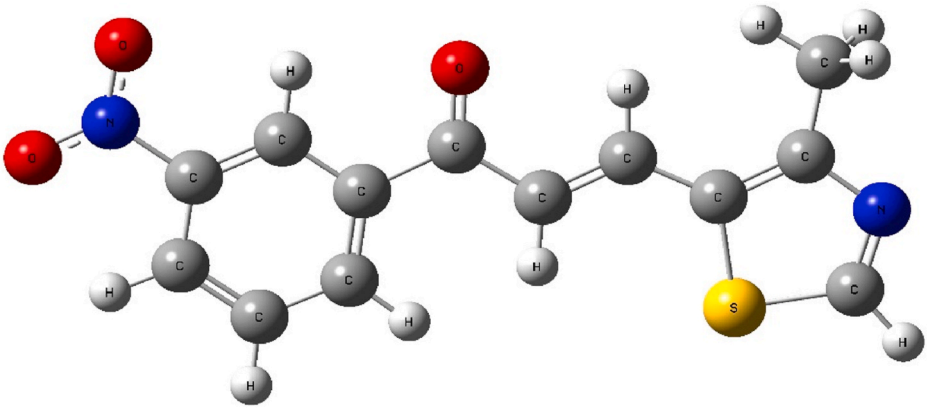

Fig. 3. Optimized structure of MNP.

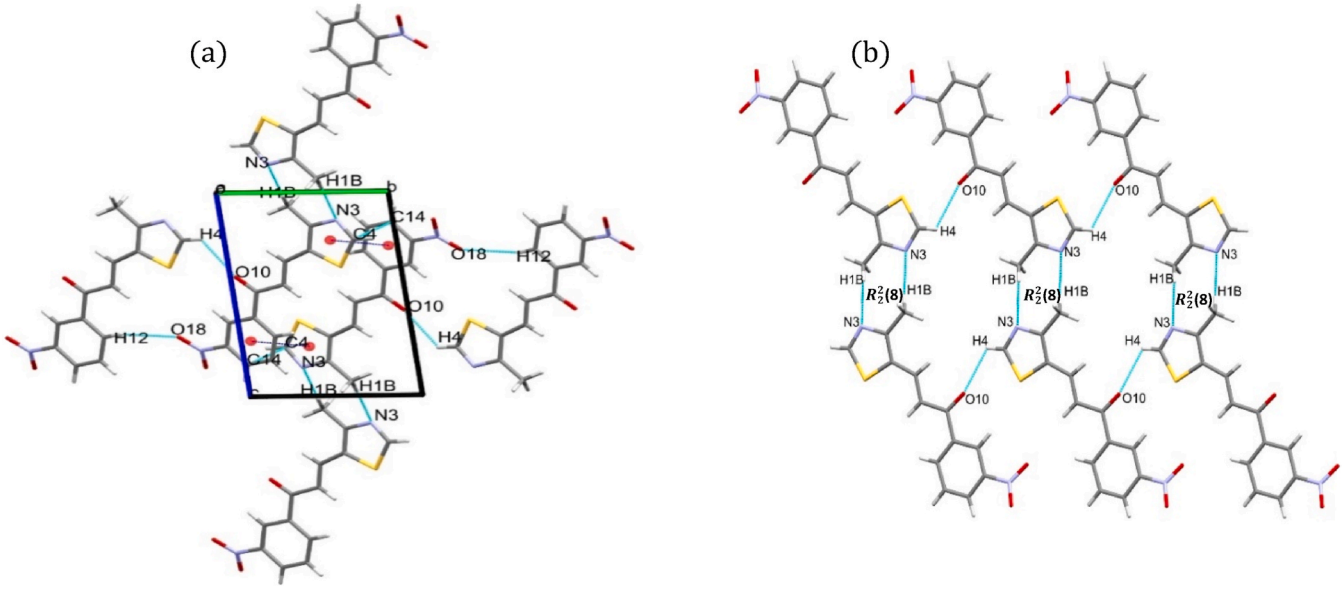

Fig. 4. Crystal packing of the title compound is shown when viewed down a-axis. (a) i) C–H···O and C–H···N interactions (shown in blue dotted lines), ii) π … π interactions (shown in red dotted lines), and (b) motif of R_2^2 (8).

Table 2
Intra and intermolecular hydrogen bonding geometry (Å, deg.) for the MNP crystal.

D–H … A	D-H	H … A	D … A	D-H … A
C12–H12···O18[a]	0.93	2.615	3.485	156.3
C1–H1B···N3[a]	0.98	2.598	3.547	171.01
C4–H4···O10[a]	0.93	2.543	3.088	115.95
C7–H7···O10[b]	0.93	2.370	2.744	103.70
C8–H8···S5[b]	0.93	2.937	3.252	101.48
C14–H14···O19[b]	0.93	2.491	2.740	95.42

[a] Intermolecular interaction.
[b] Intramolecular interaction.

C–H in-plane are predicted to occur at 1282 and 1244 cm^{-1}, showing remarkable consistency with the FT-IR bands observed at a strong intensity around 1230 cm^{-1}. In the literature [57], it is reported that the C–C–C in-plane bending vibration occurs within the range of 1000 to 600 cm^{-1}, and showed a theoretical absorption at 972 cm^{-1} with a 29 % PED. The DFT calculations predict asymmetric O–C–C stretching vibrations at 599 cm^{-1} with 29 % of PED. The nitro group displays two strong stretching vibrations: symmetric vibrations typically occurs between 1300 and 1390 cm^{-1}, while asymmetric vibrations are commonly

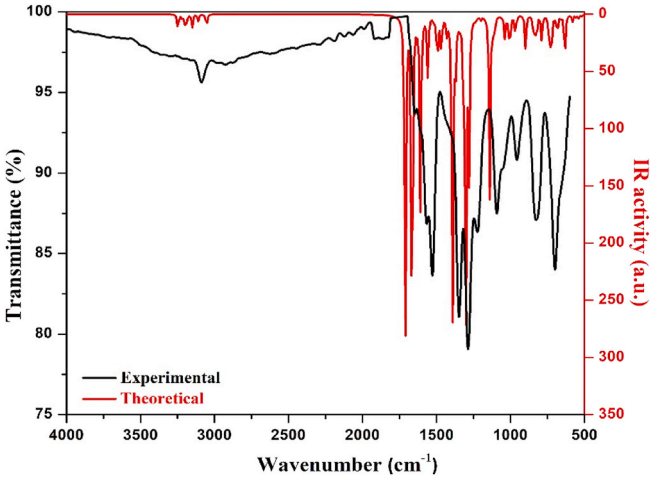

Fig. 5. Experimental and theoretical FTIR spectrum of MNP.

Table 3
Selected comparison of experimental and calculated vibrational assignments of MNP.

Wavenumber cm^{-1}			Vibrational Assignments with PED ≥10 %
Experimental	DFT		
	Unscaled	Scaled	
3094	3149	3017	ν CH (82)
1800	1706	1682	ν OC (88)
1657	1659	1589	ν CN (55)
1574	1603	1536	ν ON (34)
1532	1554	1489	ν CC (38)
	1467	1405	ν NC (30)
1346	1385	1327	ν ON (43)
	1338	1282	β HCC (53)
1284	1270	1217	β HCN (20)
1230	1299	1244	β HCC (41)
1101	1133	1085	ν NC (12)
	1054	1010	δ CCNC (12)
	1015	972	β CCC (29)
	998	956	γ HCCC (61)
959	959	919	β CNC (21)
	840	805	ν SC (30)
821	816	782	γ HCNC (93)
	782	749	β ONO (33)
	769	737	δ OCON (33)
697	655	627	γ CNCC (39)
	625	599	β OCC (24)
	550	527	β SCN (17)
	532	510	β ONC (50)
	509	488	γ SCNC (56)
	453	434	δ NCCC (18)
	419	401	β CCN (27)

found in the range of 1500–1600 cm^{-1} [58,59]. In our molecule, we have identified strong absorption bands at 1574 cm^{-1} corresponding to the asymmetric stretching band and at 1346 cm^{-1} for the symmetric stretching band of the nitro group within the nitrophenyl group. Theoretical assignments place these vibration bands at 1536 cm^{-1} and 1327 cm^{-1} with a 34% and 43% PED contribution respectively. The torsional vibration of the thiazole (C=N–C–C) bond was experimentally observed at 697 cm^{-1}, whereas the calculated value at 627 cm^{-1}. Furthermore, the calculated (S–C) stretching vibration was determined to be 805 cm^{-1}.

3.3. Optical studies

3.3.1. Optical bandgap and refractive index calculation

The optical characteristics of the MNP crystal were studied through UV–Vis–NIR spectrum analysis employing a Beckman Coulter-DU-730 UV–Vis–NIR spectrophotometer, within the wavelength range of 300–800 nm, encompassing the 200–400 nm (UV region), and 400–800 nm (visible region). The sample was prepared by using ethanol as the solvent. The MNP crystal showed 97.85% of transmittance at 800 nm (See Fig. 6a). Fig. 6a displays the transmittance spectrum of the MNP crystal, revealing that at 365 nm, the UV cut-off wavelength is detected. The notable high transmittance in the crystal suggests minimal crystal defects, indicating reduced optical losses within the crystal. These kinds of crystals are well-suited for NLO applications. The MNP crystal's linear absorption coefficient (α) was obtained using the following formula [60]:

$$\alpha = \frac{2.3026}{t} \log \frac{1}{T} \tag{6}$$

Here, T represents the transmittance, and 't' denotes the sample thickness. The determination of the optical band gap energy (E_g) is facilitated through Tauc plot relations [61], which is shown below;

$$\alpha h\upsilon = C\,(h\upsilon - E_g)^n \tag{7}$$

In the above Equation, E_g, C, and hυ represent the optical band gap, material constant, and photon energy, respectively. The parameter n in Equation (7) characterizes the different types of electronic transitions. Generally, the values 1/2, 2, 3/2, and 3 directly correlate with distinct transition types: 1/2 for direct allowed transitions, 2 for indirect allowed transitions, 3/2 for direct forbidden transitions, and 3 for indirect forbidden transitions [62]. The optical band gap (E_g) of the MNP molecule is calculated by plotting $(\alpha h\upsilon)^2$ against hυ (photon energy), as illustrated in Fig. 6b. E_g is derived by extending the linear portion of the graph to the X-axis (i.e., $\alpha = 0$). Therefore, the E_g of the MNP was measured to be 3.23 eV.

The linear refractive index (n_0) is a fundamental optical material property in materials science, due to its significant association with the material's local field and the ion electronic polarizability, both crucial factors that impact the material's optical characteristics and behavior. The linear optical properties namely, reflectance (R), linear refractive index (n_0), and extinction coefficient (K) of the MNP were determined. Also, the linear refractive index is an essential parameter for determining third-order NLO parameters. The values of n_0, K, and, R determined utilizing the corresponding mathematical expressions [63] as shown below:

$$K = \frac{\alpha\lambda}{4\pi} \tag{8}$$

$$R = \frac{\exp(-\alpha t) \pm \sqrt{\exp(-\alpha t)T - \exp(-3\alpha t)T + \exp(-2\alpha t)T^2}}{\exp(-\alpha t)T + \exp(-2\alpha t)T} \tag{9}$$

$$n_0 = \frac{-(1+R) \pm 2\sqrt{R}}{(1-R)} \tag{10}$$

Here, α and t are the same as mentioned in equation (7). The parameter 'K' characterizes the light absorption behavior of chemical species at a particular wavelength, thereby exerting a direct impact on the material's linear refractive index. The variation of the extinction coefficient (K) and refractive index (n_0) with wavelength, as illustrated in Fig. 6c and d, provides valuable insights into the optical properties of the MNP. The observed high value of extinction coefficient at 364 nm indicates substantial light absorption due to electronic transitions, while the low extinction coefficient values at longer wavelengths (around 800 nm) suggest high transparency and minimal defects, which are beneficial for nonlinear optical (NLO) applications [64]. The refractive index (n_0), calculated using Equation (10), was found to be 1.58 at 532 nm, underscoring the material's suitability for high-performance NLO activities [65]. This refractive index value is crucial for determining the third-order nonlinear optical susceptibility ($\chi^{(3)}$) of the MNP. Overall, these optical properties highlight the MNP's potential for advanced photonic applications.

3.3.2. TD-DFT absorption calculations

To explore the electronic absorption characteristics of the MNP compound, we utilized a time-dependent method at three distinct theoretical levels: B3LYP, CAM-B3LYP, and wb97xd, utilizing a 6–311++G(d) basis set. These computational analyses were conducted in a solvent environment (Ethanol) utilizing the Polarizable Continuum Model (PCM) incorporating the Integral Equation Formalism variant (IEFPCM). The optimized MNP's absorption spectrum computed at three different methods, is depicted in Fig. 7. We determined the excitation energies from the ground state to each excited state. Moreover, we compared the theoretically calculated absorption spectra with the experimentally obtained ones. The calculated maximum absorption peaks of MNP at the TD-B3LYP/6-311+G(d) method were observed at 332 and 260 nm, which are close to the experimentally measured value of 343 nm. The investigation using time-dependent DFT uncovers that the absorption peaks at 332 nm and 260 nm arise from electron transitions: HOMO→LUMO+1 (91 %) and HOMO-6→LUMO (87 %),

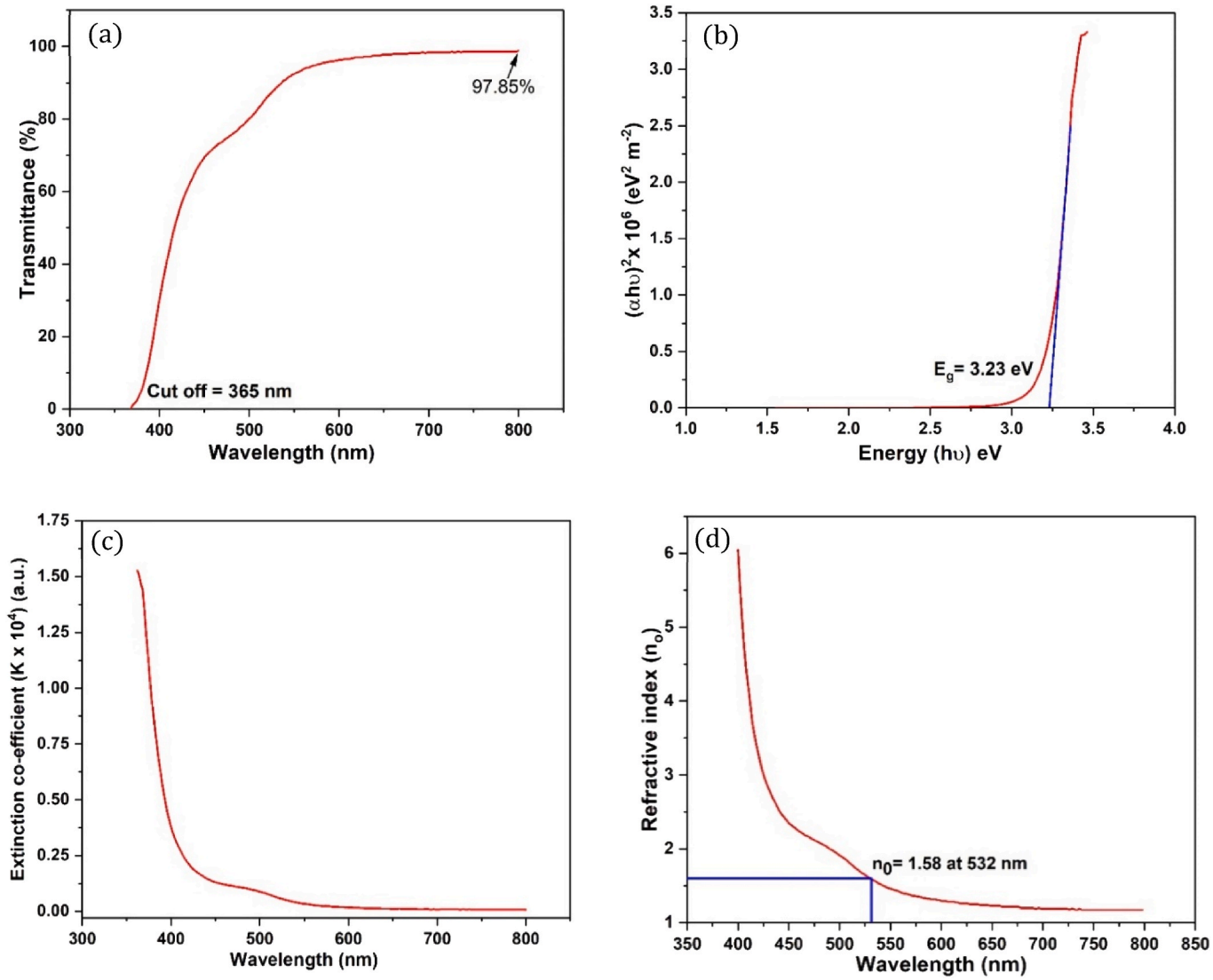

Fig. 6. (a) UV–Vis–NIR transmission spectrum, (b) Tauc's plot of the MNP crystal), (c) Variation of extinction coefficient (K) with wavelength (λ), (d) Variation of n_0 versus λ.

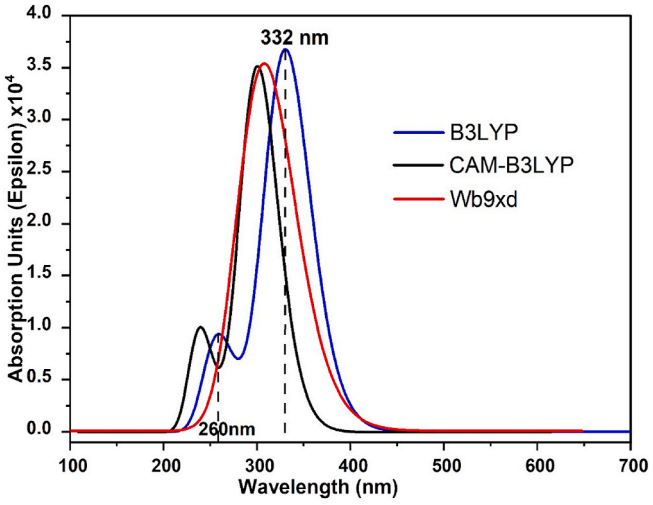

Fig. 7. Theoretical UV–vis absorption spectrum under the TD-DFT method at different levels of theory with a 6–311++G(d) basis set.

Table 4
Experimental and calculated results of UV–Vis absorption of MNP using TD-DFT/B3LYP method.

Experimental Wavelength (nm)	λ_{ex} (nm)	*E* (eV)	*f*	Major transitions
343	332.50	3.72	0.9068	HOMO→L+1 (91 %)
–	260.38	4.76	0.128	HOMO-6→LUMO (87 %)

respectively. Detailed UV–Vis absorption results for the MNP molecule, including both experimental and computed data, are presented in Table 4.

3.3.3. *Photoluminescence studies*

The production of good-quality and defect-free NLO crystals presents a formidable challenge for researchers. Laboratory-grown single crystals often exhibit elevated levels of defects and impurities in comparison to their naturally occurring crystals. Considering the wide-ranging applications of MNP crystals in photonics, it is imperative to investigate the origins of impurities and defects, as well as their effects on electronic properties. Such understanding is pivotal for refining growth parameters

and achieving defect-free crystals with favorable optical properties. Photoluminescence spectroscopy is an optical technique employed to analyze defects, study band edge peaks, and explore the crystals' electronic properties. In the present investigations, the MNP's PL spectrum was captured at ambient temperature using an F-7000 FL Spectrophotometer with an excitation wavelength of 340 nm, as observed in Fig. 8. The studied crystal consists of multiple conjugated C]C bonds (i.e., Benzene derivative) having delocalized π-electrons. The C]C bonds exhibit unique energy differences between their ground and excited states, leading to the emission of various radiation modes within the visible spectrum [66]. Fig. 8 reveals that the high-intense emission peak was observed at 435 nm, corresponding to an energy gap of 2.8 eV, which is in the blue wavelength region of the visible spectrum and there was no any additional peak observed in the spectrum, indicating the excellent crystalline perfection of the growing MNP crystal. This emission peak characterizes π–π* electronic transitions, attributed to the presence of π-electrons in carbon double bonds [67]. Moreover, the Commission Internationale de l'Eclairage (CIE) diagram provides a visual representation of the major emission peak, accentuating the predominant color. In this diagram, the higher emission peak was plotted onto the CIE coordinates (X, Y), unveiling a blue emission color that spans the entire visible range of the electromagnetic spectrum. The corresponding coordinates (X, Y) of the MNP compound were identified as (0.21578, 0.21943), as illustrated in Fig. 8. In conclusion, the results of the PL studies suggest that the MNP crystal holds potential for applications in blue light-emitting diodes.

3.4. TG-DTA analysis

The MNP compound's thermal properties were investigated using thermogravimetric (TG) and differential thermal analysis (DTA). The investigations were conducted utilizing a NETZSCH STA 449F3 thermal analyzer within a controlled nitrogen atmosphere, encompassing temperatures from 30 to 1400 °C, with a heating rate of 20°C/min. The TG/DTA curve derived from these experiments is illustrated in Fig. 9. The MNP sample was thermally stable up to 186.62°C. Initially, the TGA curve showed no significant weight loss, with only a minor weight loss observed below 186.62°C, likely due to the release of adsorbed water molecules. A sharp endothermic peak was detected at 282.91°C, corresponding to the material's melting point. The presence of this sharp and well-defined endothermic peak at 282.91°C indicates the sample's high purity and crystalline nature [68]. Another notable endothermic peak at 370.81°C suggests a phase transition before melting. The decomposition of the MNP compound occurs in different phases. In the first phase, a

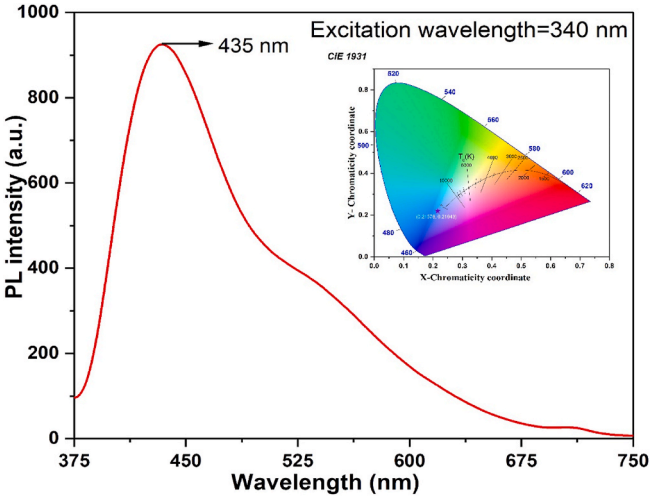

Fig. 8. PL spectrum (inset is the CIE chromaticity coordinates of an emission spectrum) of MNP.

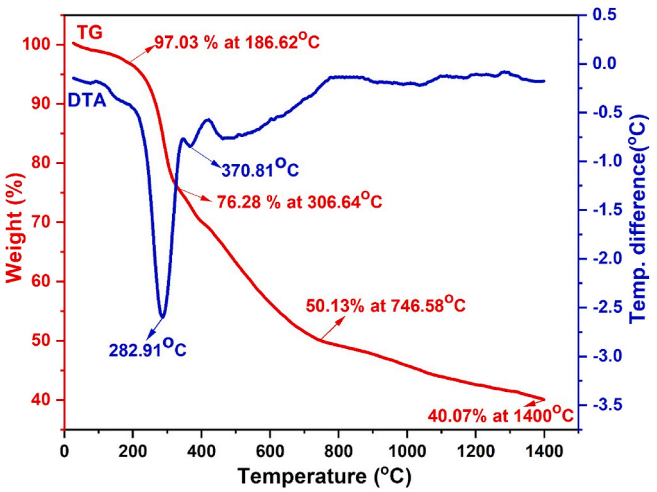

Fig. 9. TG-DTA curve of MNP molecule.

clear endothermic peak observed on the DTA curve correlates with the TG graph showing a weight loss (20.75%) between 186.62°C and 306.64°C, which is associated with the decomposition of CH_3 and CO groups [69]. The second phase of weight loss occurs between 306.64°C and 746.58°C, with an approximate weight loss of 26.15%, indicating the maximum rate of decomposition in this temperature range. In the final phase, a 10.06% weight loss was observed between 746.58°C and 1400°C. The final residue at the end is approximately 40.07 % by weight. The studied compound's thermal stability is compared with the other thiazole derivative molecules reported in the literature [70–73], as given in Table 5. Hence, the result of TG-DTA analysis suggested that the studied material can be used for NLO application up to 186.62°C.

3.5. Thermodynamic properties

The MNP's thermodynamic properties, including rotational constants, specific heat capacity (C_V), thermal energy (E), entropy (S), and zero point vibrational energy (ZPVE) are presented in Table S2 (supplementary material). These values were calculated at standard room temperature (298 K) and atmospheric pressure (1.00 atms) using different methods namely, B3LYP, CAM/B3LYP, and HF employing the 6–311++G(d,p) basis set. The table data reveals slightly lower values for total energy, vibrational, translational, and rotational parameters in the HF method compared to the B3LYP or CAM-B3LYP methods. Moreover, across all methods, the rotational constants and rotational temperature values remain unchanged. Using the theoretical harmonic frequencies of the MNP molecule, the statistical thermodynamic parameters, namely C_v, S, and H were calculated at temperatures ranging from 100 to 1000 K, and the resulting values are detailed in Table 6. From this table, we noticed that the increase in heat capacity, entropy, and enthalpy with increasing temperatures is associated with the heightened molecular vibration accompanying the ascending temperature.

Quadratic formulas were applied to fit correlation equations relating to heat capacities, entropies, enthalpy changes, and temperatures. The

Table 5
Comparison of thermal stability of MNP with reported organic molecule.

Compound	Thermal stability (°C)	References
MNP	186.62	Present work
2BTFBA	130	[70]
2BTBA	110	[70]
p-PhTT	200	[71]
BTDPA	200	[72]
BTMT	233	[73]

Table 6
Thermodynamic properties of MNP compound at different temperature.

T (K)	S (J/mol.K)	Cp (J/mol.K)	ddH (kJ/mol)
100	380.875	124.385	8.261
200	488.717	195.781	24.227
298	580.614	269.370	47.057
300	582.285	270.736	47.557
400	669.923	340.277	78.187
500	752.341	398.577	115.231
600	829.311	445.418	157.519
700	900.892	482.892	204.002
800	967.422	513.218	253.859
900	1029.354	538.117	306.466
1000	1087.154	558.822	361.343

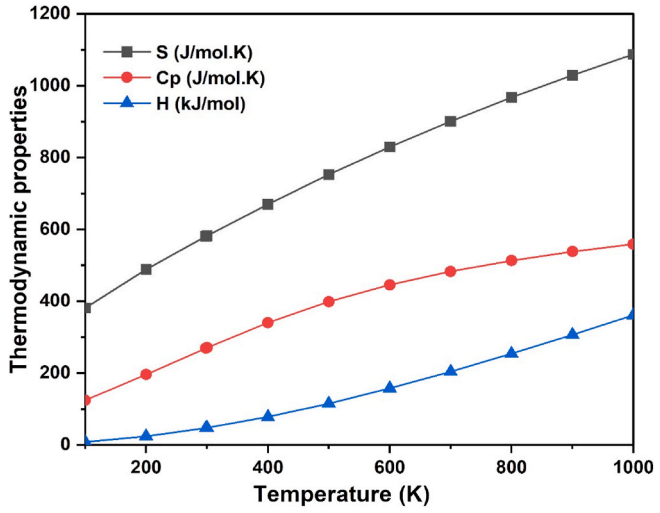

Fig. 10. Correlation graph of thermodynamic properties at different temperatures for MNP.

fitting factors (R^2) corresponding to these thermodynamic properties were found to be 0.99698, 0.97986, and 0.98785, respectively. Fig. 10 displays the correlation plots, accompanied by the corresponding fitting equations outlined below:

$$S = 279.10 + 1.088T - 0.00028\ T^2\ (R^2 = 0.99698)$$

$$Cp = 31.346 + 0.926T + 0.00040T^2\ (R^2 = 0.97986)$$

$$H = -11.659 + 0.133T + 0.00024T^2\ (R^2 = 0.98785)$$

The provided thermodynamic data offer significant utility for future research on the MNP compound. They facilitate the calculation of additional thermodynamic energies (i.e., Gibbs free energies) and support the estimation of chemical reaction directions by the second law of thermodynamics within the realm of the thermochemical field. Noted that all computations were conducted in the gaseous phase, precluding their application to solutions.

3.6. Natural Bond Orbital (NBO) analysis

NBO method stands as a pivotal tool in analyzing interactions between chemical bonds and investigating charge transfer phenomena within molecular systems. Its significance lies in its capacity to offer detailed insights into interactions involving both occupied and virtual orbitals, thereby enhancing our understanding of intra and intermolecular bonding dynamics. Furthermore, NBO analysis enables precise characterization of changes in charge densities within proton donor and acceptor orbitals, with a particular focus on bonding and antibonding orbitals. This analytical prowess highlights the importance of NBO methodology in unraveling complex molecular structures and their electronic properties, thus contributing significantly to the field of chemical research. The stabilizing donor-acceptor interactions manifest through the delocalization of electron density between lone pair orbitals and Rydberg orbitals (i.e., occupied Lewis and unoccupied non-Lewis NBO orbitals). To quantitatively assess these interactions, the stabilization energy $E^{(2)}$ is employed. This energy is determined via an analysis of the Fock matrix utilizing second-order perturbation theory within the NBO framework. The formula utilized for estimating the stabilizing energy $E^{(2)}$ pertinent to electron delocalization between each donor NBO (i) and acceptor NBO (j) is outlined as follows:

$$E^{(2)} = \Delta E_{ij}^{(2)} = q_i F^2(i,j) \Big/ \varepsilon_j - \varepsilon_i \quad (11)$$

In the above equation, q_i represents the occupancy of the donor orbital, and F (i, j) stands for the off-diagonal NBO Fock matrix. Meanwhile, εi and εj denote the diagonal elements (orbital energies). A greater $E^{(2)}$ value signifies a more pronounced interaction between the electron donor and acceptor, suggesting an increased inclination for electron transfer from the donor to the acceptor, as well as enhanced conjugation within the molecular system. Utilizing Gaussian 09 software at the B3LYP/6–311++ G(d,p) level, the NBO calculation for the MNP molecule was conducted, and the notable findings are summarized in Table 7.

The outcomes of our investigation reveal that intermolecular charge transfer (ICT) interactions involving π orbitals yield the most pronounced stabilization energy, either through the LP to π* or π to π* pathways. Notably, the interaction with the highest energy level is observed in the LP(2)O19→π*(N17–O18) transition, exhibiting a stabilization energy ($E^{(2)}$) value of 669.230 kJ/mol. Furthermore, our investigation identifies several noteworthy π to π* overlapping interactions within the molecular system. Specifically, we observe interactions such as: π(C1–C2) →[π*(C3–C4), π*(C5–C6)], π(C3–C4)→[π*(C1–C2), π*(C5–C6), π*(N17–O18)], π(C5–C6)→[π*(C1–C2), π(C3–C4), π*(C7–O9)], and π(C8–C10)→[π*(C7–O9), π*(C11–C12)], with $E^{(2)}$ values 78.533, 91.420, 89.286, 69.789, 104.6, 73.847, 94.265, 47.572, 81.588, and 52.551 kJ/mol, respectively. The important delocalization in the molecule is indicated by the electron density of the two conjugated systems. For example, the intra-molecular hyperconjugation interaction of σ[(C11–S15) and (C10–H25)] distribute to σ*[(C12–C16) and (C11–S15)] with $E^{(2)}$ of 23.095 and 25.480 kJ/mol. In addition, the charge transfer of lone pair LP (2) of the O9 and O18 atom to antibonding orbitals [σ*(C5–C7), σ*(C7–C8)] and σ*(C3–N17) showed $E^{(2)}$ of 86.483, 75.772 and 51.170 kJ/mol respectively. Similarly, the lone pair transition of LP (2) of the S15 atom to π*[(C11–C12) and (N13–C14)] showed considerable $E^{(2)}$ of 75.646 and 124.683 kJ/mol. Thus, the NBO findings indicate that the MNP molecule has strong donor-acceptor interactions suggesting good NLO properties [74].

3.7. Frontier molecular orbitals (FMO) and global chemical descriptors (GCRD)

The FMO energies for MNP in its ground state were determined using the B3LYP/6-311G++(d,p) theoretical approach. Fig. 11 provides a comprehensive visual depiction of both occupied and unoccupied molecular orbitals, elucidating their roles in facilitating electronic transitions within the MNP molecule. Highest Occupied Molecular Orbital (HOMO) and the Lowest Unoccupied Molecular Orbital (LUMO) are fundamental parameters that profoundly influence the chemical behavior and stability of molecules. This study investigates their pivotal roles in governing molecular reactivity and kinetic stability. As outlined in existing literature, the HOMO functions as an electron acceptor, acting as a nucleophile, while the LUMO serves as an electron donor, functioning as an electrophile. The energy gap between these orbitals is a critical determinant of a molecule's chemical stability [75]. Beyond its stability implications, this gap significantly influences molecular

Table 7
Selected Lewis and non-Lewis interactions from Second order perturbation theory analysis of Fock matrix for MNP molecule.

Donar NBO (i)	ED (i)(e)	Acceptor NBO (j)	ED (j)(e)	$E^{(2)}$ kJ/mol	ΔE^{a} a.u.	F (i,j)[b] a.u.
π (C1–C2)	1.6423	π* (C3–C4)	0.3425	78.5336	0.28	0.065
		π* (C5–C6)	0.3426	91.4204	0.28	0.070
π (C3–C4)	1.6410	π* (C1–C2)	0.2912	89.2865	0.29	0.071
		π* (C5–C6)	0.3426	69.7891	0.29	0.062
		π* (N17–O18)	0.6158	104.6	0.14	0.058
π (C5–C6)	1.6274	π* (C1–C2)	0.2912	73.8476	0.28	0.064
		π* (C3–C4)	0.3425	94.26552	0.28	0.071
		π* (C7–O9)	0.1855	47.57208	0.28	0.053
σ (C10–H25)	1.9679	σ*(C11–S15)	0.0291	25.4805	0.73	0.060
π (C8–C10)	1.8341	π* (C7–O9)	0.1855	81.588	0.30	0.068
		π* (C11–C12)	0.3306	52.55104	0.29	0.056
σ (C11–S15)	1.9744	σ*(C12–C16)	0.0208	23.09568	1.07	0.069
π (C11–C12)	1.7717	π* (C8–C10)	0.1414	75.1864	0.31	0.068
		π* (N13–C14)	0.3263	53.1786	0.26	0.053
π (N13–C14)	1.8668	π* (C11–C12)	0.3306	82.67584	0.34	0.077
LP (2) O9	1.8900	σ*(C5–C7)	0.0699	86.4832	0.67	0.106
		σ*(C7–C8)	0.0527	75.77224	0.71	0.102
LP (1) N13	1.8978	σ*(C14–S15)	0.0623	59.87304	0.57	0.081
LP (2) S15	1.6235	π* (C11–C12)	0.3306	75.6467	0.27	0.063
		π* (N13–C14)	0.3263	124.6832	0.24	0.077
LP (2) O18	1.8974	σ*(C3–N17)	0.1047	51.17032	0.56	0.074
LP (2) O19	1.4492	π* (N17–O18)	0.6158	669.2308	0.14	0.137

[a] Energy difference between donor orbital (i) and acceptor (j) orbital ΔE = E(i)-E(j) a.u.
[b] F (i,j) is the Fock matrix element between i and j NBO orbitals in the a.u unit.

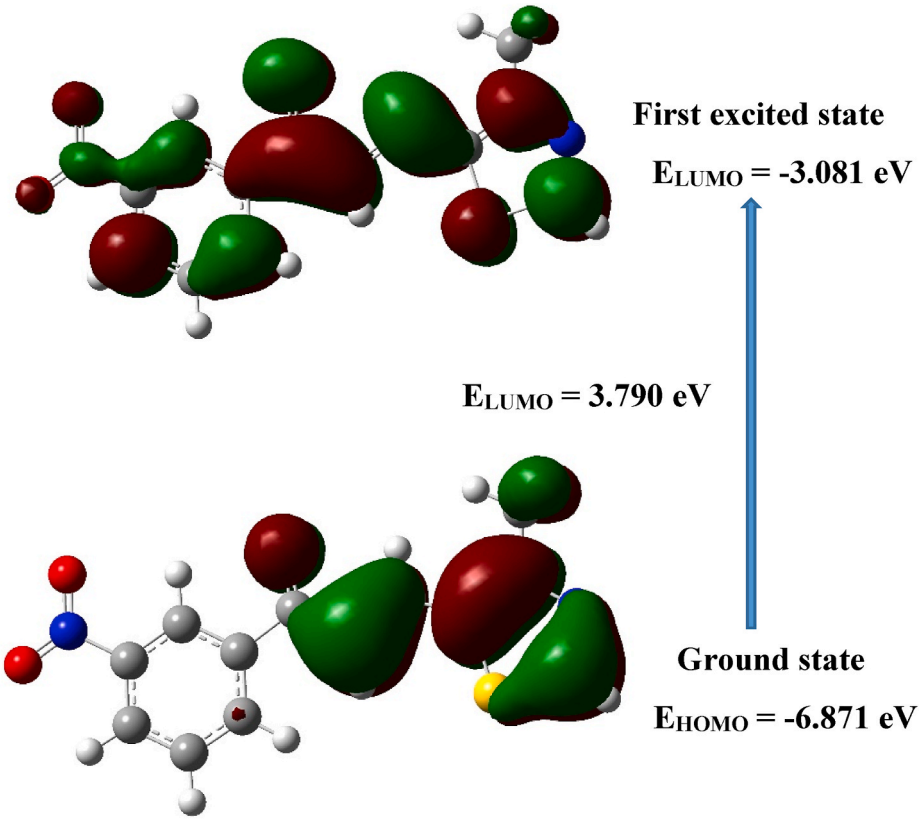

Fig. 11. Frontier molecular orbitals plot for MNP.

electrical transport properties and the measurement of electron conductivity. Table 8 shows the computed HOMO and LUMO values, as well as other global chemical descriptor values for the MNP molecule. A smaller energy gap indicates good chemical reactivity, while a larger energy gap signifies greater kinetic stability [76]. For the MNP molecule, the energy gap was measured at 3.790 eV, indicating that the studied molecule has good chemical stability and enhanced nonlinear optical activities. Fig. 11 shows molecular orbitals densities are present in the MNP molecule. Except for the nitrobenzene ring, the HOMO localizes throughout the entire molecule. The LUMO density, on the other hand, is localized on a nitrobenzene ring, thiazole ring and an oxygen atom.

Using HOMO-LUMO energies (i.e., FMO's energies), the global chemical descriptors parameters can be calculated. The GCRD parameters encompass ionization potential (I), electron affinity (A), global hardness (η), softness (S), chemical potential (μ), electronegativity (χ),

Table 8
FMO's energies with global reactivity descriptor properties.

Properties	Symbol and formula	Values
E_{HOMO}	E_H (eV)	−6.871
E_{LUMO}	E_L (eV)	−3.081
$\Delta E_{LUMO-HOMO}$	$E_g = E_{L-H}$ (eV)	3.790
Ionization potential (I)	$I = -E_{HOMO}$ (eV)	6.871
Electron affinity (A)	$A = -E_{LUMO}$ (eV)	3.081
Global Hardness (η)	$\eta=(E_{LUMO}- E_{HOMO})/2$ (eV)	1.895
Softness (S)	$S = 1/2\eta$ $(eV)^{-1}$	0.263
Chemical potential (μ)	$\mu =(E_{LUMO} + E_{HOMO})/2$ (eV)	−4.976
Electronegativity (χ)	$\chi = -\mu$ (eV)	4.976
Electrophilicity (Ψ)	$\Psi = \mu^2/2\eta$ (eV)	6.533

electrophilicity (Ψ), each defined by their respective equations as outlined below [77]:

$I = -E_{HOMO}$ (eV),

$A = -E_{LUMO}$ (eV),

$\eta = (E_{LUMO}- E_{HOMO})/2$ (eV),

$S = 1/2\eta$ $(eV)^{-1}$,

$\mu = (E_{LUMO} + E_{HOMO})/2$ (eV),

$\chi = -\mu$ (eV) and $\Psi = \mu^2/2\eta$ (eV).

The parameters mentioned above have been computed and are displayed in Table 8. The determination of a chemical hardness value of 1.89 eV, alongside a softness of 0.263 eV^{-1}, suggests the presence of charge transfer phenomena within the MNP molecular system. Additionally, the MNP compound's chemical stability is underscored by its chemical potential (μ) and an electrophilicity index (Ψ), which were computed and found −4.976 eV, and 6.533 eV respectively. The computed global reactivity descriptor properties indicate that the MNP compound exhibits notable stability and good chemical potency.

3.8. Molecular electrostatic potential (MEP)

A visual representation of the MEP for MNP is depicted in Fig. 12. This MEP map serves as a valuable tool for elucidating the molecule's reactive sites and inherent polarity. Within the MNP molecule, the potential ranges from $-4.842x10^{-2}$ to $4.842x10^{-2}$. The map illustrates the molecule's potentials using a color gradient, ranging from red to yellow, green, and finally blue, in ascending order (i.e., red < yellow < green < blue) [78]. Notably, the red-shaded regions surrounding the oxygen atoms in the carbonyl and nitrobenzene groups, which correspond to areas of low potential, signify the electrophilic nature of these atoms. In contrast, the hydrogen atoms in the thiazole and nitrobenzene rings are encircled by intensely blue-colored regions, indicating their nucleophilic nature.

3.9. Solvatochromic studies

3.9.1. Solvent effects on absorption and fluorescence spectra of MNP

The UV–visible absorption and fluorescence spectra of MNP were recorded at ambient temperature in different solvents with different polarities. Fig. 13a–b depict the absorption and emission spectra of a studied compound in selected solvents. Detailed spectral data for each solvent are summarized in Tables 9 and 10. Solvent parameters namely dielectric constant, polarity, and polarizability play a vital role in position, changes in intensity, and size of absorption and fluorescence spectra. As observed in Fig. 13a–b, the studied compound shows a broad absorption band extending from 335 to 357 nm from methanol to DMSO. Whereas, its emission spectrum also exhibits a broad emissions band ranging from 428 to 447 nm from acetonitrile to methanol, which originated from π to π^* and n to π^* transition taking place between the electron donor and the electron acceptor group, highlighting the ICT properties [79]. In Fig. 13b, it is evident that as the polarity of the solvent increases, the fluorescence emission peak experiences a bathochromic shift, affirming a $\pi\rightarrow\pi^*$ transition. The shift towards longer wavelengths in the fluorescence emission peak occurs when the excited state charge distribution of the solute differs significantly from its ground state charge distribution and interacts more intensely with polar solvents [44]. Conversely, the minor shift observed in the absorption spectra across all solvents suggests that the energy distribution of the ground state remains relatively unchanged compared to the excited state. This phenomenon is likely due to the less polar nature of the nitrobenzene derivative in its ground state. The significant change in emission indicates that the dipole moment of the excited state surpasses that of the ground state. In such instances, the relaxed excited state experiences energetic stabilization, resulting in a notable redshift in fluorescence [80].

In conclusion, the emission spectra exhibit greater sensitivity to solvent polarity, than absorption spectra. This sensitivity underscores the occurrence of photoinduced ICT within the singlet excited state, facilitated by the transfer of charge from the electron-donating group to the electron acceptor carbonyl (C=O) group of the chromophore. Moreover, the polar solvents ability to stabilize the highly dipolar excited state assists in the existence of π-π* transitions in the MNP compound. We observe that the intensity of MNP's emission spectra

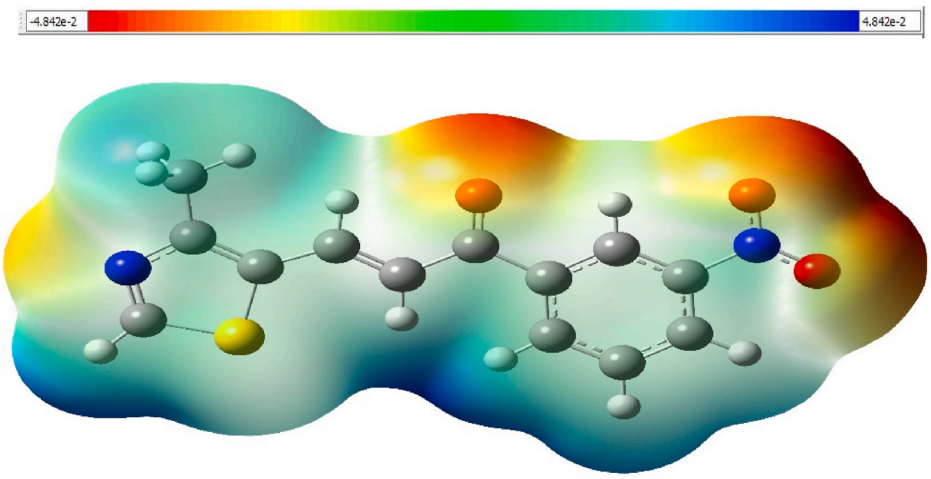

Fig. 12. The molecular electrostatic potential surface.

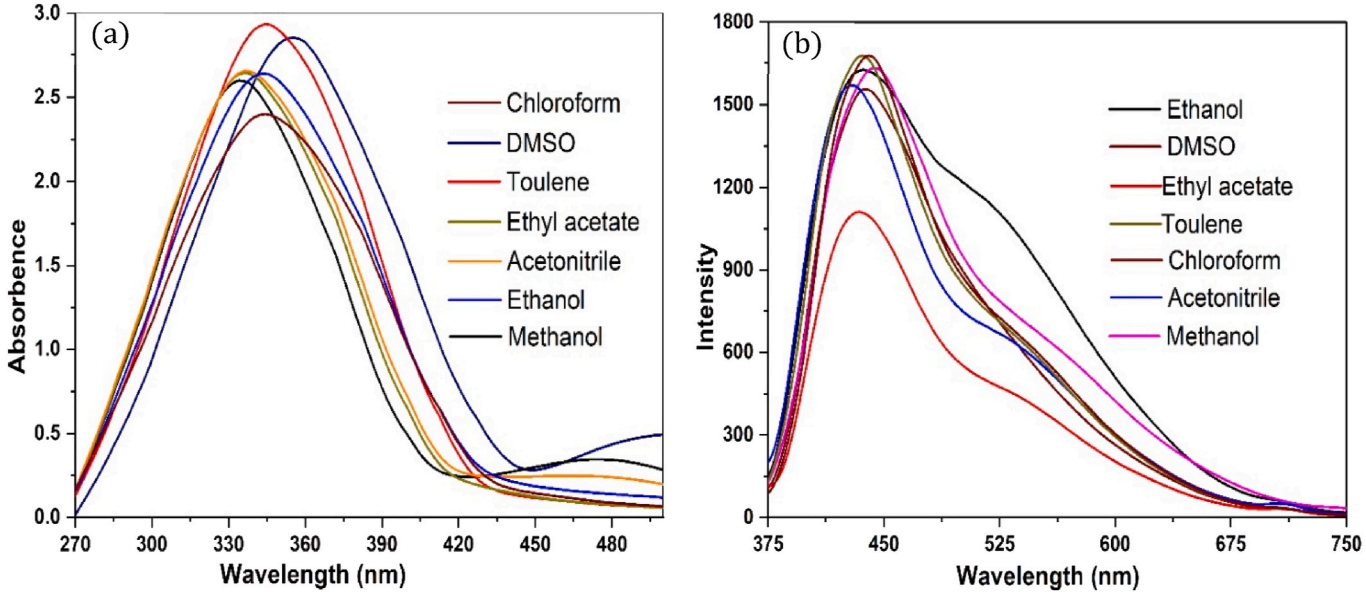

Fig. 13. (a) Absorption and (b) Emission spectra in different solvents for MNP.

Table 9
Experimental photophysical properties of MNP.

Solvents	λ^a_{abs} (nm)	λ^b_{abs} (cm^{-1})	λ^c_{emi} (nm)	λ^d_{emi} (cm^{-1})	FWHM (nm)	$\varepsilon^e \times 10^3$ Lmol $^{-1}$ cm^{-1}	f^g_{abs}
Ethanol	343	29154	437	22883	90	5.30	0.187
DMS	357	28011	438	22831	91	5.72	0.192
Toluene	345	28985	435	22988	88	5.86	0.201
Methanol	335	29850	447	22371	80	5.20	0.171
Acetonitrile	337	29673	428	23364	86	5.34	0.186
Ethyl acetate	337	29673	435	22988	84	5.31	0.182
Chloroform	346	28901	442	22624	94	4.80	0.175

[a]Absorption maxima in nm.
[b]Absorption maxima in cm^{-1}.
[c]Emission maxima in nm.
[d]Absorption maxima in cm^{-1}.
[g]Oscillator strength.
[e]Molar extinction coefficient at absorption maxima.

Table 10
Transition dipole moment (μ_{eg}), polarizability (α_{CT}), first and second hyperpolarizability (β_{CT} and γ_{CT}) of the MNP compound.

Solvents	μ^2_{eg} x 10^{-35}e. s.u	α_{CT} x 10^{-24}e. s.u	β_{CT} x 10^{-28}e. s.u	γ_{CT} x 10^{-32}e. s.u
Ethanol	1.36	4.69	2.30	1.00
DMS	1.45	5.21	2.65	1.20
Toluene	1.47	5.10	2.51	1.13
Methanol	1.22	4.11	1.96	0.84
Acetonitrile	1.33	4.51	2.17	0.92
Ethyl acetate	1.30	4.42	2.12	0.90
Chloroform	1.28	4.46	2.20	0.96

varies significantly across solvents, with maximal intensity observed in nonpolar solvents and minimal intensity in polar solvents, owing to solute-solvent interactions, particularly hydrogen bonding. Furthermore, the experimental photophysical parameters including molar extinction coefficient (ε), full-width half maximum (FWHM), transition dipole moment (μ_{eg}), and oscillator strength (f) of the MNP molecule in different solvents, were computed and listed in Table 9.

3.10. Nonlinear optical (NLO) studies

Contemporary researchers consider organic nonlinear optical chromophores a compelling area of exploration. D-π-A molecules exhibit a marked polarization of electron clouds, indicative of ICT between end groups, thereby enhancing the molecule's NLO properties. Experimental determination of NLO properties typically involves sophisticated and expensive techniques such as electric field induced second harmonic generation (EFISH) and hyper-Rayleigh scattering (HRS) at specific wavelengths [81,82]. Additionally, two other methods are there, one is the solvatochromic method and the other is the DFT computational method, which offers primary insights into the NLO properties of organic molecules through spectroscopic data analysis and computational modeling, respectively. Our study leveraged both techniques, employing the solvatochromic and DFT methods to investigate the NLO behavior of the MNP molecule and also found the NLO parameters (α, β, and γ) across different solvent environments.

3.10.1. Calculation of α_{CT}, β_{CT} and γ_{SD} from solvatochromic method

Linear polarizability (α_{CT}): Solvatochromic data serves as the primary source of information for comprehending the microscopic molecular mechanisms that arise from the interaction between a solute and different microenvironments. The evaluation of the α_{CT} for the synthesized MNP utilized a two-level model. The calculation of α_{CT} along with

the determination of the charge transfer state's dipole moment (μ_{eg}), was derived using the following equation [83,84];

$$\alpha_{xx} = \alpha_{ct} = 2\,\frac{\mu_{eg}^2}{E_{eg}} = 2\,\frac{\mu_{eg}^2 \lambda_{eg}}{hc} \tag{12}$$

$$\mu_{eg}^2 = \frac{3e^2h}{8\pi^2 mc} X\,\frac{f}{\upsilon_{max}} \tag{13}$$

In equations (12) and (13), the subscript 'x' refers to the direction of charge transfer, with 'c' representing the speed of light in a vacuum, λ_{eg} indicating the transition wavelength from the ground to an excited state, μ_{ge} being the transition dipole moment, 'm' denoting the electron mass, and E_{eg} signifying the energy of the ground-to-excited-state transition. The absorption frequency is represented by $\upsilon_{max} = \Delta E$, and 'e' is denoted as the electron charge. The oscillator strength (f) is calculated by integrating the absorption coefficient of the absorption band. Consequently, the values for the oscillator strength (f), molar extinction coefficient (ε), transition dipole moment (μ_{eg}), and linear polarizability (α_{CT}) of MNP are provided in Table 10. Notably, the MNP exhibits higher α_{CT} values ($5.21x10^{-24}$esu) in DMSO, while lower α_{CT} values ($4.11x10^{-24}$esu) in methanol.

First hyperpolarizability (β_{CT}): Qudar has introduced a two-level model for calculating solvent-dependent hyperpolarizability, which can be written in the following expression [85,86]:

$$\beta_{xxx} = \beta_{CT} = \frac{3}{2h^2c^2}\,\frac{\vartheta_{eg}^2 \mu_{eg}^2 \Delta\mu_{CT}}{\left(\vartheta_{eg}^2 - \vartheta_L^2\right)\left(\vartheta_{eg}^2 - 4\vartheta_L^2\right)} \tag{14}$$

Here, ϑ_L represents the incident radiation frequency, ϑ_{eg} is the transition frequency, and $\Delta\mu_{CT}$ is the difference in dipole moments from the excited state to the ground state. The value of $\Delta\mu_{CT}$ is determined using equation (13) and is derived based on MacRae's theory [87,88]. The hyperpolarizability derived by this equation signifies the dominant tensor component, β_{xxx}, emphasizing the charge-transfer transition, often denoted as β_{CT}. In the absence of laser excitation (i.e., υ_L=0), equation (14) reduces into the expression for static hyperpolarizability, which is given below;

$$\beta_{xxx} = \beta_{CT} = \frac{3}{2}\,\frac{\mu_{eg}^2 \Delta\mu_{CT}}{E_{eg}^2} \tag{15}$$

Finally, β_{CT} or β_{xxx} is determined by substituting the values of E_{eg}^2, μ_{eg}^2, and $\Delta\mu_{CT}$ into equation (15) in different microenvironments. The resulting β_{CT} values are listed in Table 10. The MNP molecule's highest and lowest first-order hyperpolarizability values were found in DMSO (i.e., 2.65×10^{-32}esu) and methanol (1.96×10^{-32}esu), respectively. The first-order hyperpolarizability values obtained through the solvatochromic method (see Table 10) rely on certain assumptions, providing only an approximate estimate of the dominant tensor component in the charge transfer direction-significant contributor to the overall hyperpolarizability. Despite their approximation, these values offer advantages over other sophisticated and expensive methods.

Second hyperpolarizability (γ_{SD}): The investigation of the molecular-level second-order hyperpolarizability $\langle\gamma\rangle_{SD}$, resulting from π-electron polarization within the non-resonant domain, initially employed a three-level model outlined in literature [89–91]. Subsequently, to enhance the efficiency of determining $\langle\gamma\rangle_{SD}$, a quasi-two-level model was adopted, utilizing density matrix formalism to derive a more streamlined and simplified expression [91].

$$\langle\gamma\rangle_{SD} = \frac{1}{E_{eg}^3}\,\mu_{eg}^2\left(\Delta\mu - \Delta\mu_{eg}^2\right) \tag{16}$$

Where μ_{ge} and E_{eg} are the same as mentioned in equation (12). The calculated $\langle\gamma\rangle_{SD}$ values for the MNP molecule in different solvents are tabulated in Table 10. Table 10 shows the MNP exhibits higher $\langle\gamma\rangle_{SD}$ values (1.20×10^{-32}esu) in DMSO, while lower $\langle\gamma\rangle_{SD}$ values (0.84×10^{-32}esu) in methanol.

3.10.2. Third-order nonlinear optical studies

In an era where technological advancements push the boundaries of innovation, the manipulation of light holds unparalleled significance across myriad domains. Among the diverse applications of light-matter interactions, optical limiting emerges as a crucial tool, offering a means to control and mitigate the adverse effects of intense light sources. Optical limiting, at its core, represents the ability to regulate the transmission or absorption of light, particularly in response to high-intensity pulses or beams. This phenomenon finds relevance in diverse scenarios, from protecting sensitive optical instruments to safeguarding human eyesight from potentially harmful laser radiation. By harnessing nonlinear optical processes within suitable materials, optical limiters exhibit a remarkable capacity to attenuate incident light, thereby preventing damage or distortion downstream. The foundation of optical limiting lies in the nonlinear optical properties of materials, wherein the response to light becomes increasingly nonlinear as the intensity rises. The expression of this nonlinear behavior occurs through mechanisms like nonlinear absorption, scattering, and refraction, all of which contribute to the attenuation of high-intensity light. By exploiting these nonlinear effects, researchers engineer materials with tailored optical limiting capabilities, paving the way for applications across various sectors, including telecommunications, laser safety, and photonic device protection. Z-Scan analysis, a powerful technique ingrained in nonlinear optics, stands as the first choice, offering researchers a window into the studies of the NLO behavior of materials. In the exploration of material properties, researchers often encounter phenomena that defy conventional linear optical theories. Nonlinear optical processes, characterized by interactions between lasers and matter that lead to nonlinear responses, are ubiquitous in numerous materials, ranging from semiconductors to biological systems. Understanding and harnessing these nonlinear effects is crucial for applications spanning from laser technology to biological imaging. In this realm, the present communication showed the suitability of MNP for optical limiting applications by investigating its nonlinear optical behavior under continuous wave laser irradiation.

A Z-scan experiment was set up using a 100 mW, CW diode-pumped solid-state laser with a wavelength of 532 nm, operating in TEM_{00} mode with a Gaussian profile. A convex lens with a focal length of 130 mm was used to further focus the laser beam along the Z-axis, generating the beam waist of 0.00293 cm, Rayleigh range (z_0) of 1.27 mm, and peak intensity of 14.78 kW/cm^2 at the focal point for the experimental setup [92]. A single mole of the MNP aqueous solution is employed for the analysis. After sonication for 15 min, the sample is moved to a glass cuvette with a 1 mm optical path length (L). As a result, the condition $z_0 < L$ for the thin sample approximation is met. The transmittance intensity of the Z-translated sample was measured in two Z-scan modes: closed-aperture (CA) and open-aperture (OA). The CA mode considers both nonlinear absorption and refraction, while the OA mode only measures nonlinear absorption. The ratio between CA and OA patterns reflects the extent of nonlinear refraction. Fig. 14a, b, and 14c display the CA, OA, and ratio of CA to OA Z-Scan patterns of MNP. The collected data is represented by spherical dots, and the theoretical estimate is shown by the solid line described by equations (18)–(20). The material's intrinsic self-defocusing behavior is evident as it exhibits maximum intensity prior to reaching the focal point, followed by a gradual decrease as it progresses towards positive Z positions. The negative focal length observed in the induced lens highlights the material's negative NLO attributes. Continuous-wave (CW) lasers can induce various nonlinear optical effects due to their constant light output. One significant effect is the thermal effect, which results from the absorption of laser light by the medium and the subsequent conversion of this light into heat. Although the Z-scan experiment doesn't exactly tell us the origin of optical nonlinearity, there is plenty of scientific evidence to suggest that CW

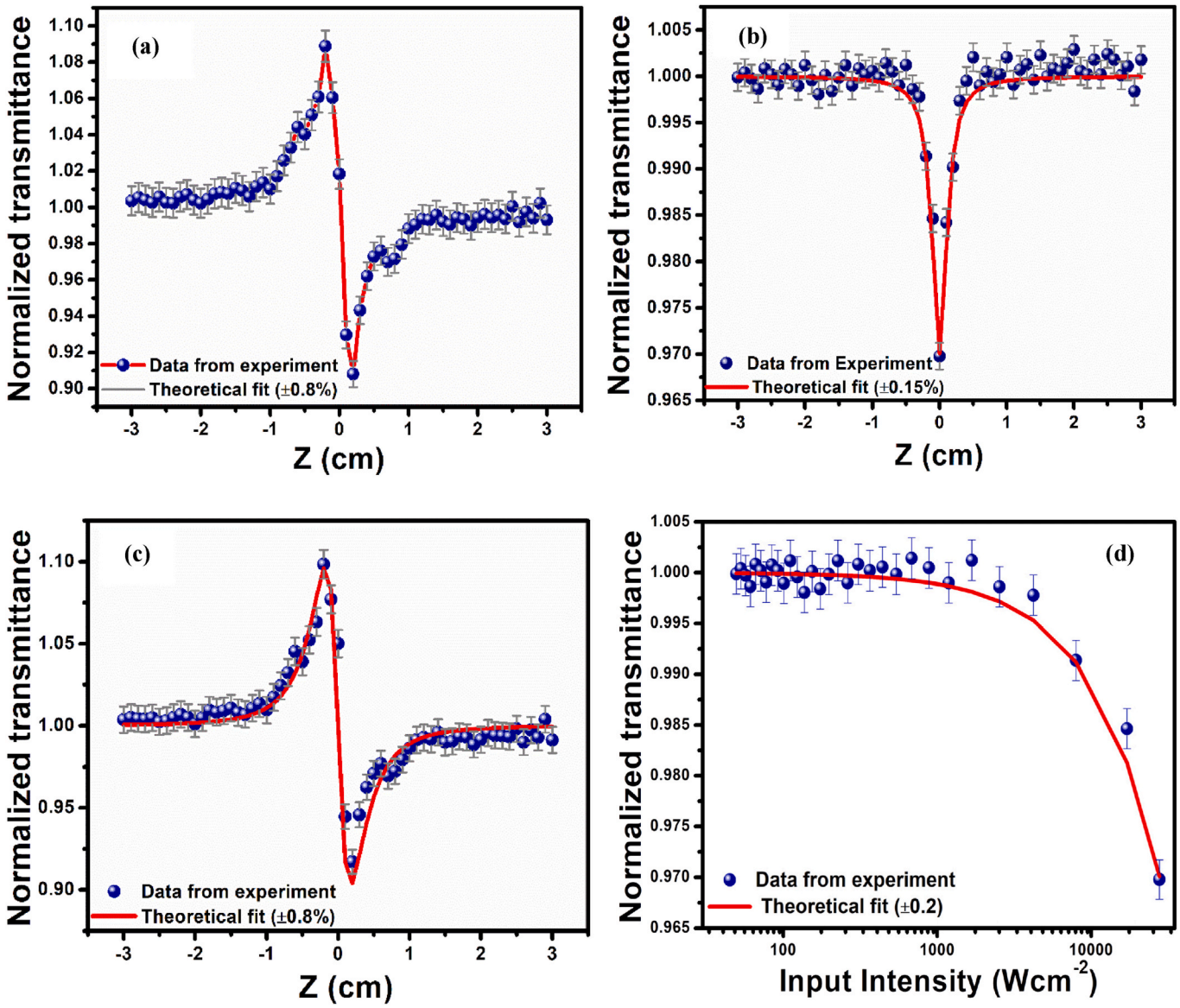

Fig. 14. (a) Closed, (b) open, (c) closed to open aperture Z-scan patterns and (d) optical limiting pattern of MNP.

laser excitation leads to thermally generated nonlinear optical effects [93,94]. These effects can include thermal lensing, thermo-optic coefficient, thermal birefringence, thermal expansion, nonlinear absorption, and self-action effects [95–97]. The self-defocusing signature of the Z-scan experiment supports the idea that optical nonlinearity in the experiment is of thermal origin. To determine the nonlinear refractive index the peak-to-valley difference $(\Delta T_{p-\upsilon})$ is utilized, and it is correlated with the on-axis phase shift (Δϕ) via an empirical relationship established by Sheik-Bahae et al. [98].

$$\Delta T_{p-\upsilon} = 0.406\ (1 - S)^{0.25}\ |\Delta\phi| \tag{17}$$

The linear aperture transmittance is mathematically expressed as S = 1- exp $(-2\, r_a^2/\omega_a^2)$, where r_a and ω_a represent the aperture radius and beam radius respectively. By fitting experimental data to an established relation [98], the Δϕ value was found to be 0.48±0.001.

$$T_{CA} = \frac{4x\Delta\varphi}{(1+x^2)\,(9+x^2)} \tag{18}$$

The following Equation (19) was utilized to calculate the magnitude of the nonlinear refractive index;

$$n_2 = \frac{\Delta\varphi}{KI_0L_{eff}}\ (cm^2\ /\ W) \tag{19}$$

Where K=2π/λ represents the wave vector, I_0 refers to the laser intensity, $L_{eff} = 1 - e^{(-\alpha_0 t)}/\alpha_0$ representing the sample's effective thickness and α_0 denotes the linear optical absorption. The magnitude of the n_2 of MNP was measured at (1.356±0.02)×10^{-8} cm^2W^{-1}, considering the described experimental setup and laser configuration.

Conversely, the Z-scan pattern acquired under open aperture circumstances shows the reverse saturable absorption (RSA), validating the appropriateness of the MNP material for effective optical limiting (OL) purposes. The MNP's nonlinear absorption coefficient was determined through curve fitting analysis utilizing the data from the OA Z-scan and the corresponding equation given as,

$$T_{OA} = \frac{1}{1 + \left(\beta \times L_{eff}\left[\frac{I_0}{1+x^2}\right]\right)} \tag{20}$$

In the above equation, β represents the nonlinear absorption coefficient, I_0 and L_{eff} is same as equation (19). Therefore, the magnitude of β for

MNP is determined as $(1.03\pm0.04)\times10^{-4}$ cmW^{-1}. The relationship between the β and n_2 is established through their connection to the real and imaginary parts of the third-order nonlinear susceptibility ($\chi^{(3)}$) using the following relation [99].

$$\chi_R^{(3)} = \frac{10^{-4}\left(\varepsilon_0 c^2 n_0^2 n_2\right)}{\pi}\ (\mathrm{cm}^2/\mathrm{W}) \tag{21}$$

$$\chi_I^{(3)} = \frac{10^{-2}\left(\varepsilon_0 c^2 n_0^2 \lambda\beta\right)}{4\pi^2}\ (\mathrm{cm}/\mathrm{W}) \tag{22}$$

$$\chi^{(3)} = \sqrt{\left(\chi_R^{(3)}\right)^2 + \left(\chi_I^{(3)}\right)^2}\ (\mathrm{esu}) \tag{23}$$

The values n_2, β, and $\chi^{(3)}$ have been compiled in Table 11. Errors in a Z-scan experiment can arise from various sources. Some common reasons for possible errors are beam alignment, sample quality, positioning errors, laser stability, detector sensitivity, thermal effects, and polarization effects. However, much effort has been made to avoid such errors during the experiments through careful experimental design, calibration, and control of environmental conditions to minimize these errors and improve accuracy. Comparing NLO parameters with existing literature can be complex due to variations in material properties, measurement wavelengths, intensities, and experimental setups. For accurate comparisons, it's crucial to use consistent experimental procedures. In our study, the third-order nonlinear susceptibility $\chi^{(3)}$ of the MNP compound was measured as 3.01×10^{-6} esu. This value is notably higher than those reported for other organic NLO materials [63,96, 99–104], as summarized in Table 12. This finding indicates that the MNP compound exhibits a superior nonlinear optical response compared to existing materials, underscoring its potential for advanced photonic applications [105].

MNP is a compound with intriguing third-order nonlinear optical properties. These properties stem from its molecular structure, which exhibits conjugated aromatic rings and functional groups capable of participating in nonlinear optical processes. The molecule has an abundance of delocalized π-electrons, which significantly boost its nonlinear optical behaviour through self-phase modulation. This modulation causes a nonlinear phase shift in light passing through a medium, leading to spectral broadening and the creation of new frequencies. Additionally, the structural stability of the molecule is enhanced by its donor-hydrogen-acceptor configuration, which promotes charge delocalization through a push-pull mechanism. This, in turn, leads to improved nonlinear optical absorption and, ultimately, enhances the optical limiting capability. Moreover, materials demonstrating reverse saturable absorption can serve as optical limiters by exhibiting reduced transmittance as input intensity increases. Fig. 14d displays the optical limiting curve of MNP, illustrating the normalized transmittance against the input intensities. The position-dependent input intensity values are computed using the below relation,

$$I(z) = 4\sqrt{\ln 2}\left(\frac{E_{in}}{\pi^{3/2}\,\omega(z)^2}\right) \tag{24}$$

Table 11
Third-order nonlinear optical parameters of MNP.

Parameters	Values
Nonlinear refractive index (n_2)	$(1.356 \pm 0.02) \times 10^{-8}$ cm^2 W^{-1}
Nonlinear absorption coefficient (β)	$(1.03 \pm 0.04) \times 10^{-4}$ cm W^{-1}
Real part of third-order nonlinear optical susceptibility (Re (χ^3))	$(8.57 \pm 0.082) \times 10^{-7}$ esu
Imaginary part of third-order nonlinear optical susceptibility (Im (χ^3))	$(2.89 \pm 0.06) \times 10^{-6}$ esu
Third-order nonlinear optical susceptibility ($\chi^{(3)}$)	$(3.01 \pm 0.04) \times 10^{-6}$ esu
Optical limiting threshold value	$(4.213 \pm 0.2) \times 10^{-31}$ esu

Table 12
Comparison of $\chi^{(3)}$ values of MNP with reported nonlinear optical materials.

Molecules	Third order susceptibility ($\chi^{(3)}$)	References
MNP	3.01×10^{-6} esu	Present work
CT	0.87×10^{-6} esu	[99]
FAMFC	0.21×10^{-6} esu	[100]
BCA	2.43×10^{-6} esu	[63]
A5CP5	4.201×10^{-7} esu	[101]
4AP4NP	1.80×10^{-8} esu	[102]
2APB	2.91×10^{-8} esu	[96]
AAP	6.20×10^{-9} esu	[103]
P2CNB	4.428×10^{-10} esu	[104]

Where $\omega(z) = \omega_0^2\,[1 + (z/z_0)^2]$ and ω_0 is the beam radius [92]. The material shows a calculated onset optical limiting threshold value of $(4.213\pm0.2)\times10^3$ Wcm^{-2} for 532 nm indicating that this material is a strong contender for optical limiting applications. The value of the optical limiting threshold was calculated by fitting the experimental data using equation (24). After reviewing the literature, we found reports on optical limiting investigations of organic molecules using the Z-scan technique with a 532 nm under CW laser. Notably, S. Ananda et al. [63, 77,106] and Pratheba et al. [99,107] have reported optical limiting thresholds of 2.511×10^3 Wcm^{-2} for CDA [77], 3.437×10^3 Wcm^{-2} for BCA [63], 7.632×10^3 Wcm^{-2} for 4MBA [106] and 3.44×10^3 Wcm^{-2} for 4MPB [99]. Our findings indicate that the MNP compound's optical limiting threshold value is well within the range of these reported values under similar experimental conditions (532 nm CW laser).

3.10.3. Computational NLO

To understand the NLO behavior of any material, it is essential to understand its molecular properties, including dipole moments (μ), polarizability (α), and hyperpolarizabilities (β and γ). In this context, quantum chemical calculations are pivotal for understanding electronic structures and establishing correlations with NLO behavior. In this study, we present the computed values of static dipole moments (μ), static and dynamic polarizabilities (α), and hyperpolarizabilities (β and γ) at different input frequencies namely; ω = 0 a.u., ω = 0.04282 a.u., ω = 0.05695 a.u., and ω = 0.08564 a.u. Detailed results are provided in Tables 13–15. Upon observation, all tensor components exhibited non-zero values in a specific direction. The axial x-components, including polarizability (α_{xx}), first and second hyperpolarizabilities (β_{xxx} and γ_{xxxx}), were identified as dominant longitudinal components, supported by their mean values. The predominant contribution originating from the x-component towards the average values provides evidence for charge transfer interaction occurring along the X-axis in the MNP compound [108]. Strong donor-acceptor configuration in the molecular system resulted in a high value of dipole moment (μ). The calculated dipole moment for the studied molecule was found to be 7.012 Debye.

The MNP's tensor components along the x, y, and z axis have been employed for computing the static polarizability [α(0; 0)] at λ = 0 (ω = 0 a.u.). Additionally, three different wavelengths have been used to estimate the dynamic polarizability [α(-ω; ω)], with λ = 1064 nm, 800 nm, and 532 nm, respectively. The obtained values are presented in Table 13. From Table 13, the static isotropic (α_{total}) and anisotropic polarizability (Δα) were found to be 2.63×10^{-23} esu and 6.65×10^{-23} esu and these values are 5.35 and 32.92 times larger than the corresponding values for the urea molecule ($\alpha_{tot} = 0.49102\times10^{-23}$ esu and $\Delta\alpha = 0.2020006\times10^{-23}$ esu) [109]. The dynamic values of α_{total} and Δα at three different frequencies, namely, ω = 0.08564, ω = 0.05695 and ω = 0.04282 are 2.867×10^{-23} esu, 2.727×10^{-23} esu, and 2.686×10^{-23} esu, and 7.273×10^{-23} esu, 6.894×10^{-23} esu, and 6.783×10^{-23} esu, respectively. Notably, the dynamic α_{total} and Δα values are observed to be higher than static values. These results highlight the direct influence of incident frequencies on the MNP's polarizability [106].

The augmentation of intra-charge transfer and resonant effect within the MNP molecule heightens the second-order nonlinearity,

Table 13
Dipole moment, static and dynamic polarizability by TDHF at 6-31G of MNP.

Dipole moment (μ)		Polarizability (α)				
Components	Values (Debye)	Components	ω = 0	ω = 0.04282 λ = 1064 nm	ω = 0.05695 λ = 800 nm	ω = 0.08564 λ = 532 nm
μ_x	4.574	α_{xx}	279.73	287.41	293.88	316.24
μ_y	−5.257	α_{xy}	−9.07	−10.08	−10.97	−14.26
μ_z	0.782	α_{yy}	176.85	178.89	180.54	185.76
		α_{xz}	4.43	4.52	4.60	4.87
μ_{total}	7.012	α_{yz}	−5.48	−5.58	−5.67	−5.94
		α_{zz}	70.71	70.93	71.11	71.63
		α_{total} a.u.	175.76	179.08	181.84	191.21
		$\alpha_{total} \times 10^{-23}$ esu	2.63	2.68	2.72	2.86
		Δα a.u.	443.39	452.22	459.61	484.81
		Δα × 10^{-23} esu	6.65	6.78	6.89	7.27

Table 14
The static and dynamic first-order hyperpolarizability by TDHF/6- 311G level.

Components	ω = 0	ω = 0.04282 λ = 1064 nm	ω = 0.05695 λ = 800 nm	ω = 0.08564 λ = 532 nm
β_{xxx}	671.23	1094.09	1731.63	67621.01
β_{xyy}	181.44	249.49	338.88	7098.09
β_{xzz}	−16.62	−21.02	−27.21	−595.05
β_{yyy}	60.51	51.71	36.07	−1602.60
β_{yzz}	22.26	24.14	26.34	167.73
β_{yxx}	−725.69	−935.93	−1198.20	−17896.23
β_{zzz}	−0.93	−1.02	1.15	−9.26
β_{zxx}	68.91	84.15	101.94	1047.89
β_{zyy}	−21.39	−22.09	−22.38	62.45
β_x	836.06	1322.56	2043.30	74124.05
β_y	−642.91	−860.07	347.74	−19331.11
β_z	46.58	61.03	80.72	1101.08
β a.u.	1055.70	1578.80	2074.25	76611.22
β × 10^{-30} esu	9.12	13.64	17.92	66.92

Table 15
The static second hyperpolarizability γ(0; 0,0,0) and frequency-dependent second hyperpolarizability γ(-3ω; ω, ω, ω) at 6-311G method (TDHF).

Components	ω = 0	ω = 0.04282 λ = 1064 nm	ω = 0.05695 λ = 800 nm	ω = 0.08564 λ = 532 nm
γ_{xxxx}	169643.13	469184.97	142284822.40	3588119424.00
γ_{yyyy}	4354.51	6682.27	698051.96	31863935.83
γ_{zzzz}	239.03	277.59	217.88	−7067.13
γ_{xxyy}	15329.28	36083.56	9163762.08	311390756.30
γ_{xxzz}	616.45	1135.60	154798.35	−22288928.60
γ_{yyzz}	433.43	573.27	23619.47	−2216914.14
γ a.u.	41399.00	110345.94	32333490.42	838749224.00
γ × 10^{-36} esu	20.86	55.61	162.96	4227.10

contributing to the behavior of the first hyperpolarizability parameter. The static β (0; 0, 0) for the studied molecule was found to be 9.121×10^{-30} esu which is 17.78 times larger than the urea molecule (0.51286×10^{-30} esu). The dynamic β(-2ω; ω, ω) is computed at three different frequencies and the values are 66.920×10^{-30} esu at ω = 0.08564, 17.921×10^{-30} esu at ω = 0.05695, and 13.640×10^{-30} esu at ω = 0, 0.04282, which are 91.03, 24.378 and 18.55 times larger than the urea molecule (0.73512×10^{-30} esu) [110]. The static and dynamic first-order hyperpolarizability values are presented in Table 14.

The MNP molecule's static and dynamic second-order hyperpolarizability tensor components (γ(0; 0, 0, 0) and, γ(3ω; ω, ω, ω)), have been computed at frequencies ω = 0, 0.04282, 0.05695, and 0.08564, as detailed in Table 15. The molecular γ values are contingent upon various factors, including the π-electron conjugation, the molecule's dimensionality, and the nature of substituents. The presence of a donor-acceptor π-conjugated bridge system in MNP facilitates charge transfer via the phenyl rings from the substituent groups, thereby influencing the NLO properties. The phenyl rings play a crucial bridging role, particularly in the presence of donor-acceptor substituents, contributing significantly to the non-zero values observed for both static and dynamic hyperpolarizabilities in the MNP molecule, reflecting microscopic NLO responses [111]. The calculated γ(0; 0, 0, 0), for the studied molecule is found to be 20.865×10^{-36} esu. Similarly, the dynamic γ(3ω; ω, ω, ω), is calculated at various wavelengths: λ = 1064 nm λ = 800 nm, and λ = 532 nm respectively, and the results are tabulated accordingly in Table 15. Notably, as the applied frequency rises, there is a concurrent increase in the dynamic second-order hyperpolarizability. Finally, the outcomes observed for the MNP molecule appear potential in NLO applications.

4. Conclusion

In summary, a good-quality, optically transparent MNP, an organic NLO crystal was synthesized and grown using the slow evaporation solution method. Single crystal XRD studies revealed that MNP crystallized in the *P*-1 space group. The MNP's optical properties were investigated using UV–Vis analysis, unveiling a high transparency and low absorption in the visible spectrum, with a cut-off wavelength determined to be 365 nm. Additionally, utilizing reflectance data and Tauc's relation, the crystal's energy band gap was found to be 3.23 eV. The photoluminescence spectrum was utilized to examine crystal defects and their origin. The determination of the CIE coordinate based on the luminescence spectrum confirmed the MNP crystal's capacity for emitting blue light. The solvatochromic analysis provided insights into the crystal's polarity and its solvent response, highlighting higher α_{CT}, β_{CT}, and γ_{CT} values in polar solvents compared to nonpolar solvents. Specifically, for the MNP molecule in DMSO solvent, the higher α_{CT}, β_{CT}, and γ_{CT} values were observed and the values are 5.21×10^{-24} esu, 2.65×10^{-32} esu, and 1.20×10^{-32} esu, respectively. The computational absorption wavelength (332.50 nm) was obtained through the TD-DFT method, which was compared with the experimental absorption wavelength (343 nm). The energy gap, (i.e., $E_{HOMO\text{-}LUMO}$ = 3.79 eV), suggests a heightened presence of ICT interactions within the molecule. Moreover, a GCRD analysis highlights a notable global hardness value of 1.895 eV, affirming enhanced stability and lower chemical reactivity in the molecule. The NBO analysis revealed a significant stabilization energy of 669.230 kJ/mol, indicating ICT interactions in the MNP molecule facilitated by a strong orbital overlap between the lone pair on (O19) and the antibonding orbital of π*(N17–O18). The Z-scan experimental findings show that under CW laser irradiation at 532 nm, the materials exhibit both two-photon absorption and negative nonlinear refraction properties. The measured optical limiting value (OL) of the MNP compound, (i.e., 4.213×10^{3} Wcm^{-2}), indicates its suitability for utilization in optical limiting applications. The studied compound shows higher values of first and second hyperpolarizabilities, indicating favorable potential for nonlinear optical (NLO) behavior. Thus, the

results from various studies suggest that the MNP molecule holds promise as a significant material for applications in photonics, nonlinear optics (NLO), and electro-optics.

CRediT authorship contribution statement

Keerthikumara Venkatesha: Writing – review & editing, Writing – original draft, Visualization, Validation, Software, Resources, Methodology, Investigation, Formal analysis, Data curation, Conceptualization. **Mahesh Sankanahalli Srinivas:** Software, Investigation, Formal analysis. **Ananda Swamynayaka:** Software, Methodology, Investigation, Formal analysis, Data curation. **Mahendra Madegowda:** Writing – review & editing, Supervision, Software, Methodology, Formal analysis, Conceptualization. **Ravi Singh Krishna:** Software, Formal analysis. **Tejaswi Ashok Hegde:** Software, Methodology, Formal analysis, Data curation. **Maralinganadoddi P. Sadashiva:** Formal analysis, Data curation.

Declaration of competing interest

The authors declare that they have no known competing financial interests or personal relationships that could have appeared to influence the work reported in this paper.

Data availability

Data will be made available on request.

Acknowledgments

The author Keerthikumara V thanks to University Grants Commission (UGC), New Delhi for providing financial support (NTA-Ref. No.: 201610078208, Dated: 01-04-2021). The authors would like to thank the University with Potential for Excellence (UPE) University of Mysore for providing UV–Vis measurements and also thank SAIF, IIT-Madras for single crystal XRD analysis. We express our gratitude to Dr. Jeyaseelan S. for granting us access to the computational facility. Dr. Mahendra M woud like to thank VGST, Government of Karnataka for awarding a research grant under the head K-FIST L2 (KSTePS/VGST/GRD No. 1133/2022–23/654).

Appendix A. Supplementary data

Supplementary data to this article can be found online at https://doi.org/10.1016/j.optmat.2024.116068.

References

[1] C.C. Evans, M. Bagieu-Beucher, R. Masse, J.-F. Nicoud, Nonlinearity enhancement by solid-state proton transfer: a new strategy for the design of nonlinear optical materials, Chem. Mater. 10 (3) (1998) 847–854.
[2] J. Nicoud, R. Twieg, D. Chemla, J. Zyss, in: D.S. Chemla, J. Zyss (Eds.), Nonlinear Optical Properties of Organic Molecules and Crystals, Academic press, London, 1987, pp. 227–296.
[3] L.T. Cheng, W. Tam, S.R. Marder, A.E. Stiegman, G. Rikken, C.W. Spangler, Experimental investigations of organic molecular nonlinear optical polarizabilities. 2. A study of conjugation dependences, J. Phys. Chem. 95 (26) (1991) 10643–10652.
[4] A.K. Jain, A. Vaidya, V. Ravichandran, S.K. Kashaw, R.K. Agrawal, Recent developments and biological activities of thiazolidinone derivatives: a review, Bioorg. Med. Chem. 20 (11) (2012) 3378–3395.
[5] S. Muhammad, S. Kumar, J. Koh, M. Saravanabhavan, K. Ayub, M. Chaudhary, Synthesis, characterisation, optical and nonlinear optical properties of thiazole and benzothiazole derivatives: a dual approach, Mol. Simulat. 44 (15) (2018) 1191–1199.
[6] H.A. Khamees, M. Jyothi, S.A. Khanum, M. Madegowda, Synthesis, crystal structure, spectroscopic characterization, docking simulation and density functional studies of 1-(3, 4-dimethoxyphenyl)-3-(4-flurophenyl)-propan-1-one, J. Mol. Struct. 1161 (2018) 199–217.
[7] H.A. Khamees, M. Madegowda, S. Ananda, Y. Sangappa, F.H. Al-Ostoot, N. Abad, Synthesis, molecular structure, DFT studies, in silico docking and molecular dynamics simulations of 2, 6 dimethoxychalcone derivatives as BRD4 inhibitors, J. Mol. Struct. 1245 (2021) 131032.
[8] S.R. Maidur, P.S. Patil, S.V. Rao, M. Shkir, S. Dharmaprakash, Experimental and computational studies on second-and third-order nonlinear optical properties of a novel D-π-A type chalcone derivative: 3-(4-methoxyphenyl)-1-(4-nitrophenyl) prop-2-en-1-one, Opt Laser. Technol. 97 (2017) 219–228.
[9] S.M. Gomha, H.A. Abdel-Aziz, Synthesis of new heterocycles derived from 3-(3-methyl-1H-indol-2-yl)-3-oxopropanenitrile as potent antifungal agents, Bull. Kor. Chem. Soc. 33 (9) (2012) 2985–2990.
[10] K.D. Hargrave, F.K. Hess, J.T. Oliver, N-(4-Substituted-thiazolyl) oxamic acid derivatives, new series of potent, orally active antiallergy agents, J. Med. Chem. 26 (8) (1983) 1158–1163.
[11] W.C. Patt, H.W. Hamilton, M.D. Taylor, M.J. Ryan, D.G. Taylor Jr., C.J. Connolly, A.M. Doherty, S.R. Klutchko, I. Sircar, Structure-activity relationships of a series of 2-amino-4-thiazole-containing renin inhibitors, J. Med. Chem. 35 (14) (1992) 2562–2572.
[12] A.S. Cantrell, P. Engelhardt, M. Högberg, S.R. Jaskunas, N.G. Johansson, C. L. Jordan, J. Kangasmetsä, M.D. Kinnick, P. Lind, J.M. Morin, Phenethylthiazolylthiourea (PETT) compounds as a new class of HIV-1 reverse transcriptase inhibitors. 2. Synthesis and further structure− activity relationship studies of PETT analogs, J. Med. Chem. 39 (21) (1996) 4261–4274.
[13] M.-H. Shih, F.-Y. Ke, Syntheses and evaluation of antioxidant activity of sydnonyl substituted thiazolidinone and thiazoline derivatives, Bioorg. Med. Chem. 12 (17) (2004) 4633–4643.
[14] M.S. Alam, L. Liu, Y.-E. Lee, D.-U. Lee, Synthesis, antibacterial activity and quantum-chemical studies of novel 2-arylidenehydrazinyl-4-arylthiazole analogues, Chem. Pharm. Bull. 59 (5) (2011) 568–573.
[15] J.C. Jaen, L.D. Wise, B.W. Caprathe, H. Tecle, S. Bergmeier, C.C. Humblet, T. G. Heffner, L.T. Meltzer, T.A. Pugsley, 4-(1, 2, 5, 6-Tetrahydro-1-alkyl-3-pyridinyl)-2-thiazolamines: a novel class of compounds with central dopamine agonist properties, J. Med. Chem. 33 (1) (1990) 311–317.
[16] S.M. Gomha, T.A. Salah, A.O. Abdelhamid, Synthesis, characterization, and pharmacological evaluation of some novel thiadiazoles and thiazoles incorporating pyrazole moiety as anticancer agents, Monatshefte für Chemie-Chemical Monthly 146 (2015) 149–158.
[17] M. Zia ur Rehman, J.A. Choudary, S. Ahmad, An efficient synthesis of 2-alkyl-4-hydroxy-2H-1, 2-benzothiazine-3-carboxamide-1, 1-dioxides, Bull. Kor. Chem. Soc. 26 (11) (2005) 1771–1775.
[18] D. Lednicer, The Organic Chemistry of Drug Synthesis, vol. 7, John Wiley & Sons, 2007 vol. 8.
[19] S.R. Chemburkar, J. Bauer, K. Deming, H. Spiwek, K. Patel, J. Morris, R. Henry, S. Spanton, W. Dziki, W. Porter, Dealing with the impact of ritonavir polymorphs on the late stages of bulk drug process development, Org. Process Res. Dev. 4 (5) (2000) 413–417.
[20] J. Bauer, S. Spanton, R. Henry, J. Quick, W. Dziki, W. Porter, J. Morris, Ritonavir: an extraordinary example of conformational polymorphism, Pharmaceut. Res. 18 (2001) 859–866.
[21] A. Rouf, C. Tanyeli, Bioactive thiazole and benzothiazole derivatives, Eur. J. Med. Chem. 97 (2015) 911–927.
[22] N. Zelisko, D. Atamanyuk, O. Vasylenko, P. Grellier, R. Lesyk, Synthesis and antitrypanosomal activity of new 6, 6, 7-trisubstituted thiopyrano [2, 3-d][1, 3] thiazoles, Bioorg. Med. Chem. Lett 22 (23) (2012) 7071–7074.
[23] P. Makam, P.K. Thakur, T. Kannan, In vitro and in silico antimalarial activity of 2-(2-hydrazinyl) thiazole derivatives, Eur. J. Pharmaceut. Sci. 52 (2014) 138–145.
[24] H. Osman, A. Arshad, C.K. Lam, M.C. Bagley, Microwave-assisted synthesis and antioxidant properties of hydrazinyl thiazolyl coumarin derivatives, Chem. Cent. J. (6) (2012) 1–10.
[25] A. Ignat, T. Lovasz, M. Vasilescu, E. Fischer-Fodor, C.B. Tatomir, C. Cristea, L. Silaghi-Dumitrescu, V. Zaharia, Heterocycles 27. Microwave assisted synthesis and antitumour activity of novel phenothiazinyl-thiazolyl-hydrazine derivatives, Arch. Pharmazie 345 (7) (2012) 574–583.
[26] P. Karegoudar, M.S. Karthikeyan, D.J. Prasad, M. Mahalinga, B.S. Holla, N. S. Kumari, Synthesis of some novel 2, 4-disubstituted thiazoles as possible antimicrobial agents, Eur. J. Med. Chem. 43 (2) (2008) 261–267.
[27] P. Tejkiran, M.B. Teja, P.S.S. Kumar, P. Sankar, R. Philip, S. Naveen, N. Lokanath, G.N. Rao, DA-π-D Synthetic approach for thienyl chalcones–NLO–a structure activity study, J. Photochem. Photobiol. Chem. 324 (2016) 33–39.
[28] H. Chen, L. Wang, W.-Y. Wang, Y.-Q. Qiu, H.-M. Xie, The effect of heterocyclic π bridges on second order nonlinear optical properties of compounds formed between ferrocenyl and corannulenyl, RSC Adv. 6 (99) (2016) 97063–97069.
[29] M.C.R. Castro, M. Belsley, M.M.M. Raposo, Push–pull second harmonic generation chromophores bearing pyrrole and thiazole heterocycles functionalized with several acceptor moieties: syntheses and characterization, Dyes Pigments 128 (2016) 89–95.
[30] S. Bradamante, A. Facchetti, G.A. Pagani, Heterocycles as donor and acceptor units in push–pull conjugated molecules. Part 1, J. Phys. Org. Chem. 10 (7) (1997) 514–524.
[31] A. Facchetti, A. Abbotto, L. Beverina, M.E. van der Boom, P. Dutta, G. Evmenenko, T.J. Marks, G.A. Pagani, Azinium−(π-bridge)− pyrrole NLO-phores: influence of heterocycle acceptors on chromophoric and self-assembled thin-film properties, Chem. Mater. 14 (12) (2002) 4996–5005.
[32] A. Facchetti, A. Abbotto, L. Beverina, M.E. Van der Boom, P. Dutta, G. Evmenenko, G.A. Pagani, T.J. Marks, Layer-by-layer self-assembled pyrrole-based donor− acceptor chromophores as electro-optic materials, Chem. Mater. 15 (5) (2003) 1064–1072.

[33] A. Facchetti, L. Beverina, M.E. Van Der Boom, P. Dutta, G. Evmenenko, A. D. Shukla, C.E. Stern, G.A. Pagani, T.J. Marks, Strategies for electrooptic film fabrication. Influence of pyrrole– pyridine-based dibranched chromophore architecture on covalent self-assembly, thin-film microstructure, and nonlinear optical response, J. Am. Chem. Soc. 128 (6) (2006) 2142–2153.
[34] M.M.M. Raposo, M.C.R. Castro, A.M.C. Fonseca, P. Schellenberg, M. Belsley, Design, synthesis, and characterization of the electrochemical, nonlinear optical properties, and theoretical studies of novel thienylpyrrole azo dyes bearing benzothiazole acceptor groups, Tetrahedron 67 (29) (2011) 5189–5198.
[35] M.M.M. Raposo, A.M. Sousa, G. Kirsch, P. Cardoso, M. Belsley, E. de Matos Gomes, A.M.C. Fonseca, Synthesis and characterization of dicyanovinyl-substituted thienylpyrroles as new nonlinear optical chromophores, Org. Lett. 8 (17) (2006) 3681–3684.
[36] P.J. Coelho, L.M. Carvalho, A.M.C. Fonseca, M.M.M. Raposo, Photochromic properties of thienylpyrrole azo dyes in solution, Tetrahedron Lett. 47 (22) (2006) 3711–3714.
[37] C.S. Naveena, B. Poojary, T. Arulmoli, K. Manjunatha, A. Prabhu, N.S. Kumari, Synthesis and evaluation of biological and nonlinear optical properties of some novel 2, 4-disubstituted [1, 3]-thiazoles carrying 2-(aryloxymethyl)-phenyl moiety, Med. Chem. Res. 22 (2013) 1925–1937.
[38] K.G. Thorat, N. Sekar, Pyrrole-thiazole based push-pull chromophores: an experimental and theoretical approach to structural, spectroscopic and NLO properties of the novel styryl dyes, J. Photochem. Photobiol. Chem. 333 (2017) 1–17.
[39] C. Dirk, H. Katz, M. Schilling, L. King, Use of thiazole rings to enhance molecular second-order nonlinear optical susceptibilities, Chem. Mater. 2 (6) (1990) 700–705.
[40] E.M. Breitung, C.-F. Shu, R.J. McMahon, Thiazole and thiophene analogues of donor– acceptor stilbenes: molecular hyperpolarizabilities and structure–property relationships, J. Am. Chem. Soc. 122 (6) (2000) 1154–1160.
[41] A. Abbotto, L. Beverina, N. Manfredi, G.A. Pagani, G. Archetti, H.G. Kuball, C. Wittenburg, J. Heck, J. Holtmann, Second-order nonlinear optical activity of dipolar chromophores based on pyrrole-hydrazono donor moieties, Chem.–Eur. J. 15 (25) (2009) 6175–6185.
[42] A. Nekrouf, K. Toubal, Y. Megrouss, N.E.H. Belkafouf, A. Djafri, N. Khelloul, J.-C. Daran, A. Djafri, A. Chouaih, Synthesis, structural, spectroscopic, intermolecular interactions, kinetic stability, charge transfer method with DNA bases and electronic properties of (E)-3-(2-ethoxyphenyl)-5-(3-(2-methoxyphenyl)-4methylthiazol-2 (3H)-ylidene)-2-thioxothiazolidin-4-one: computational and experimental approach, J. Mol. Struct. 1262 (2022) 133002.
[43] R.V. Doddamani, P.S. Rachipudi, N.A. Pattanashetti, M.Y. Karidurаganavar, Synthesis, structural characterization and computational study of NLO-responsive chromophores and second-order coefficients of thermally crosslinked polymers, New J. Chem. 43 (39) (2019) 15723–15735.
[44] M. Frisch, G. Trucks, H. Schlegel, G. Scuseria, M. Robb, J. Cheeseman, G. Scalmani, V. Barone, B. Mennucci, G. Petersson, GAUSSIAN 09, Rev. C. 01, D. 01. Gaussian, Inc, Wallingford CT, 2010.
[45] M.H. Jamróz, Vibrational energy distribution analysis (VEDA): scopes and limitations, Spectrochim. Acta Mol. Biomol. Spectrosc. 114 (2013) 220–230.
[46] M. Gordon, J. Jensen, S. Koseki, N. Matsunaga, K. Nguyen, S. Su, T. Windus, Partially based on us gamess version 6 jun 1999,* us gamess versions 6 sep 2001 and 12 dec 2003* from iowa state university* mw schmidt, kk baldridge, ja boatz, st elbert, J. Comput. Chem. 14 (1993) 1347–1363.
[47] G.M. Sheldrick, Crystal structure refinement with SHELXL, Acta Crystallogr., Sect. C: Struct. Chem. 71 (1) (2015) 3–8.
[48] C.F. Macrae, I.J. Bruno, J.A. Chisholm, P.R. Edgington, P. McCabe, E. Pidcock, L. Rodriguez-Monge, R. Taylor, J. Streek, P.A. Wood, Mercury CSD 2.0–new features for the visualization and investigation of crystal structures, J. Appl. Crystallogr. 41 (2) (2008) 466–470.
[49] P. Van der Sluis, A. Spek, BYPASS: an effective method for the refinement of crystal structures containing disordered solvent regions, Acta Crystallogr., Sect. A: Found. Crystallogr. 46 (3) (1990) 194–201.
[50] L. Sutton, Tables of interatomic distances, Chemical Society M170 (1958).
[51] H.A. Khamees, K. Chaluvaiah, N.A. El-Khatatneh, A. Swamynayaka, K.H. Chong, J.P. Dasappa, M. Madegowda, Crystal structure, DFT calculation, Hirshfeld surface analysis and energy framework study of 6-bromo-2-(4-bromophenyl) imidazo [1, 2-a] pyridine, Acta Crystallogr. E: Crystallographic Communications 75 (11) (2019) 1620–1626.
[52] A.R. Guerroudj, N. Boukabcha, A. Benmohammed, N. Dege, N.E.H. Belkafouf, N. Khelloul, A. Djafri, A. Chouaih, Synthesis, crystal structure, vibrational spectral investigation, intermolecular interactions, chemical reactivity, NLO properties and molecular docking analysis on (E)-N-(4-nitrobenzylidene)-3-chlorobenzenamine: a combined experimental and theoretical study, J. Mol. Struct. 1240 (2021) 130589.
[53] B.N. Revanna, M. Madegowda, Dithiane based boronic acid as a carbohydrate sensor in an aqueous solution at pH 7.5: theoretical and experimental approach, J. Fluoresc. 31 (6) (2021) 1683–1703.
[54] B.H. Stuart, Infrared Spectroscopy: Fundamentals and Applications, John Wiley & Sons, 2004.
[55] V. Balachandran, A. Janaki, A. Nataraj, Theoretical investigations on molecular structure, vibrational spectra, HOMO, LUMO, NBO analysis and hyperpolarizability calculations of thiophene-2-carbohydrazide, Spectrochim. Acta Mol. Biomol. Spectrosc. 118 (2014) 321–330.
[56] M. Kandasamy, G. Velraj, S. Kalaichelvan, G. Mariappan, Characterization of 1, 5-dimethoxynaphthalene by vibrational spectroscopy (FT-IR and FT-Raman) and density functional theory calculations, Spectrochim. Acta Mol. Biomol. Spectrosc. 134 (2015) 191–199.
[57] D. Lin-Vien, N.B. Colthup, W.G. Fateley, J.G. Grasselli, The Handbook of Infrared and Raman Characteristic Frequencies of Organic Molecules, Elsevier, 1991.
[58] S.E. Krikorian, M. Mahpour, The identification and origin of NH overtone and combination bands in the near-infrared spectra of simple primary and secondary amides, Spectrochim. Acta Mol. Spectros 29 (7) (1973) 1233–1246.
[59] T. Miyazawa, Internal rotation and low frequency spectra of esters, monosubstituted amides and polyglycine, Bull. Chem. Soc. Jpn. 34 (5) (1961) 691–696.
[60] T.A. Hegde, A. Dutta, R.M. Jauhar, P. Karuppasamy, M.S. Pandian, M. Abith, T. S. Girisun, G. Vinitha, Physicochemical properties of cesium tetroxalate dihydrate single crystal: an efficient material for nonlinear optical applications, Opt. Mater. 107 (2020) 110033.
[61] J. Tauc, R. Grigorovici, A. Vancu, Optical properties and electronic structure of amorphous germanium, Phys. Status Solidi 15 (2) (1966) 627–637.
[62] S. Nandhini, K. Sudhakar, S. Muniyappan, P. Murugakoothan, Systematic discussions on structural, optical, mechanical, electrical and its application to NLO devices of a novel semi-organic single crystal: guanidinium tetrafluoroborate (GFB), Opt Laser. Technol. 105 (2018) 249–256.
[63] A. Swamynayaka, K. Venkatesha, K.K. Harish, B.N. Revanna, C. Venkatesh, M. Madegowda, T.A. Hegde, Third-order nonlinear response of a novel organic acetohydrazide derivative: experimental and theoretical approach, Opt. Mater. 139 (2023) 113826.
[64] T.S. Girisun, S. Dhanuskodi, Linear and nonlinear optical properties of tris thiourea zinc sulphate single crystals, Cryst. Res. Technol.: Journal of Experimental and Industrial Crystallography 44 (12) (2009) 1297–1302.
[65] J.K. Zaręba, D. Mayer, M. Samoć, R.A. Fischer, Nonlinear Optical Properties, Upconversion and Lasing in Metal–Organic Frameworks, 2017.
[66] S.R. Devi, S. Kalaiyarasi, I.M. Zahid, R.M. Kumar, Studies on the growth aspects, structural, thermal, dielectric and third order nonlinear optical properties of solution grown 4-methylpyridinium p-nitrophenolate single crystal, J. Cryst. Growth 454 (2016) 139–146.
[67] J. Dalal, N. Sinha, H. Yadav, B. Kumar, Structural, electrical, ferroelectric and mechanical properties with Hirshfeld surface analysis of novel NLO semiorganic sodium p-nitrophenolate dihydrate piezoelectric single crystal, RSC Adv. 5 (71) (2015) 57735–57748.
[68] H. Purandara, S. Raghavendra, S. Foro, P. Patil, B.T. Gowda, S. Dharmaprakash, P. Vishwanatha, Synthesis, spectroscopic characterization, crystal structure, Hirshfeld surface analysis and third-order nonlinear optical properties of 2-(4-chlorophenoxy)-N'-[(1E)-1-(4-methylphenyl) ethylidene] acetohydrazide, J. Mol. Struct. 1185 (2019) 205–211.
[69] K. Venkatesha, K. Sheela, M.S. Srinivas, A. Swamynayaka, M. Madegowda, T. A. Hegde, M.P. Sadashiva, Physicochemical properties of thiazole-based NLO crystal: an efficient material for optoelectronic applications, J. Mol. Struct. (2024) 139459.
[70] C. Raveendiran, P. Prabukanthan, Synthesis, crystal growth, crystal arrangement, optical, thermal, NLO and biological investigations of heterocyclic compounds of N-(1, 3-benzothiazol-2-yl) benzamide and N-(1, 3-benzothiazol-2-yl)-2-fluorobenzamide, European Journal of Engineering and Technology Research 6 (5) (2021) 181–189.
[71] U. Olgun, M. Gülfen, Synthesis of fluorescence poly (phenylenethiazolo [5, 4-d] thiazole) copolymer dye: spectroscopy, cyclic voltammetry and thermal analysis, Dyes Pigments 102 (2014) 189–195.
[72] K. Ramesh, S. Munusamy, S. Muhammad, M.S. Karthikeyan, A.G. Al-Sehemi, M. Sekar, Synthesis, characterization, and computational exploration of 6-ethoxy-2-aminobenzothiazolium diphenylacetate crystal as an efficient NLO material, J. Mater. Sci. Mater. Electron. 34 (14) (2023) 1140.
[73] E. İnkaya, Synthesis, X-ray structure, FT-IR, NMR (13C/1H), UV–Vis spectroscopy, TG/DTA study and DFT calculations on 2-(benzo [d] thiazol-2-ylthio)-1-((1s, 3s)-3-mesityl-3-methylcyclobutyl) ethan-1-one, J. Mol. Struct. 1173 (2018) 148–156.
[74] H.A. Khamees, Y.H.E. Mohammed, S. Ananda, F.H. Al-Ostoot, Y. Sangappa, S. Alghamdi, S.A. Khanum, M. Madegowda, Effect of o-difluoro and p-methyl substituents on the structure, optical properties and anti-inflammatory activity of phenoxy thiazole acetamide derivatives: theoretical and experimental studies, J. Mol. Struct. 1199 (2020) 127024.
[75] I. Fleming, Molecular Orbitals and Organic Chemical Reactions, John Wiley & Sons, 2011.
[76] R.A. Costa, P.O. Pitt, M.L.B. Pinheiro, K.M. Oliveira, K.S. Salomé, A. Barison, E. V. Costa, Spectroscopic investigation, vibrational assignments, HOMO-LUMO, NBO, MEP analysis and molecular docking studies of oxoaporphine alkaloid liriodenine, Spectrochim. Acta Mol. Biomol. Spectrosc. 174 (2017) 94–104.
[77] S. Ananda, H.A. Khamees, M. Mahendra, C. Kumara, D. Jagadeesh Prasad, T. A. Hegde, G. Vinitha, Structural, thermal, dielectric, nonlinear optical properties and DFT investigations of a novel material 2-(6-chloropyridin-3-yl)-N'-(2, 3-dihydro-1, 4-benzodioxin-6-ylmethylidene) acetohydrazide for optoelectronic applications, J. Mater. Sci. Mater. Electron. 32 (2021) 14677–14702.
[78] J. Liu, J. Wu, J. Zhu, Z. Wang, J. Zhou, K. Cen, Removal of oxygen functional groups in lignite by hydrothermal dewatering: an experimental and DFT study, Fuel 178 (2016) 85–92.
[79] P. Gogoi, U. Mohan, M.P. Borpuzari, A. Boruah, S.K. Baruah, UV-Visible spectroscopy and density functional study of solvent effect on halogen bonded charge-transfer complex of 2-Chloropyridine and iodine monochloride, Arab. J. Chem. 12 (8) (2019) 4522–4532.

[80] B. Shivaleela, G. Shivraj, S. Hanagodimath, Estimation of dipole moments by Solvatochromic shift method, spectroscopic analysis of UV–Visible, HOMO-LUMO, ESP map, Mulliken atomic charges, NBO and NLO properties of benzofuran derivative, Results in Chemistry 6 (2023) 101046.
[81] E. Benassi, F. Egidi, V. Barone, General strategy for computing nonlinear optical properties of large neutral and cationic organic chromophores in solution, J. Phys. Chem. B 119 (7) (2015) 3155–3173.
[82] C. Bosshard, G. Knöpfle, P. Prêtre, P. Günter, Second-order polarizabilities of nitropyridine derivatives determined with electric-field-induced second-harmonic generation and a solvatochromic method: a comparative study, J. Appl. Phys. 71 (4) (1992) 1594–1605.
[83] A. Abbotto, L. Beverina, S. Bradamante, A. Facchetti, C. Klein, G.A. Pagani, M. Redi-Abshiro, R. Wortmann, A distinctive example of the cooperative interplay of structure and environment in tuning of intramolecular charge transfer in second-order nonlinear optical chromophores, Chem.–Eur. J. 9 (9) (2003) 1991–2007.
[84] F. Momicchioli, G. Ponterini, D. Vanossi, First-and second-order polarizabilities of simple merocyanines. An experimental and theoretical reassessment of the two-level model, J. Phys. Chem. 112 (46) (2008) 11861–11872.
[85] B. Carlotti, R. Flamini, I. Kikaš, U. Mazzucato, A. Spalletti, Intramolecular charge transfer, solvatochromism and hyperpolarizability of compounds bearing ethenylene or ethynylene bridges, Chem. Phys. 407 (2012) 9–19.
[86] J.-L. Oudar, D.S. Chemla, Hyperpolarizabilities of the nitroanilines and their relations to the excited state dipole moment, J. Chem. Phys. 66 (6) (1977) 2664–2668.
[87] E. McRae, Theory of solvent effects on molecular electronic spectra. Frequency shifts, J. Phys. Chem. 61 (5) (1957) 562–572.
[88] S. Bruni, E. Cariati, F. Cariati, F. Porta, S. Quici, D. Roberto, Determination of the quadratic hyperpolarizability of trans-4-[4-(dimethylamino) styryl] pyridine and 5-dimethylamino-1, 10-phenanthroline from solvatochromism of absorption and fluorescence spectra: a comparison with the electric-field-induced second-harmonic generation technique, Spectrochim. Acta Mol. Biomol. Spectrosc. 57 (7) (2001) 1417–1426.
[89] J.d. Oudar, Optical nonlinearities of conjugated molecules. Stilbene derivatives and highly polar aromatic compounds, J. Chem. Phys. 67 (2) (1977) 446–457.
[90] O.-P. Kwon, M. Jazbinsek, J.-I. Seo, P.-J. Kim, E.-Y. Choi, Y.S. Lee, P. Günter, First hyperpolarizability orientation in asymmetric pyrrole-based polyene chromophores, Dyes Pigments 85 (3) (2010) 162–170.
[91] C.W. Dirk, L.T. Cheng, M.G. Kuzyk, A simplified three-level model describing the molecular third-order nonlinear optical susceptibility, Int. J. Quant. Chem. 43 (1) (1992) 27–36.
[92] T.A. Hegde, T.S. Girisun, G. Vinitha, Crystal structure and physicochemical properties of a new optofunctional metal-organic cocrystal delivering intermolecular charge-transfer-enhanced nonlinear optical and optical limiting properties, J. Mater. Sci. Mater. Electron. 32 (2021) 18669–18688.
[93] G. Muruganandi, M. Saravanan, G. Vinitha, M.J. Raj, T.S. Girisun, Barium borate nanorod decorated reduced graphene oxide for optical power limiting applications, Opt. Mater. 75 (2018) 612–618.
[94] T.S. Girisun, S. Dhanuskodi, Nonlinear optical susceptibilities of diglycinyl thiourea for frequency conversion and optical limiting applications, Chem. Phys. Lett. 491 (4–6) (2010) 248–253.
[95] M. Saravanan, S.G. Tc, G. Vinitha, Facile hydrothermal synthesis of CdFe2O4-reduced graphene oxide nanocomposites and their third-order nonlinear optical properties under CW excitation, J. Mol. Liq. 256 (2018) 519–526.
[96] T.A. Hegde, A. Dutta, T.S. Girisun, G. Vinitha, A novel chlorocadmate hybrid cocrystal delivering intermolecular charge transfer enhanced nonlinear optical properties and optical limiting, Opt. Mater. 117 (2021) 111194.
[97] R.L. Sutherland, Handbook of Nonlinear Optics, CRC press, 2003.
[98] M. Sheik-Bahae, A.A. Said, T.-H. Wei, D.J. Hagan, E.W. Van Stryland, Sensitive measurement of optical nonlinearities using a single beam, IEEE J. Quant. Electron. 26 (4) (1990) 760–769.
[99] K. Prathebha, K. Raju, T.A. Hegde, G. Vinitha, Computation and experimental results on spectroscopic and physicochemical properties of efficient piperidine driven passive optical limiting material, Phys. Scripta 97 (3) (2022) 035804.
[100] T.A. Hegde, A. Dutta, T. Sabari Girisun, M. Abith, G. Vinitha, Intensity tunable optical limiting behavior of an organometallic cesium hydrogen tartrate single crystal, J. Mater. Sci. Mater. Electron. 30 (2019) 18885–18896.
[101] J. Ranjith Emmanuel, T. Kamalesh, P. Karuppasamy, M. Senthil Pandian, P. Ramasamy, Growth of 2-amino-5-chloropyridinium 5-sulfosalicylate (2A5CP5S) single crystals: investigation of physicochemical properties for nonlinear optical applications, J. Mater. Sci. Mater. Electron. 33 (33) (2022) 25285–25296.
[102] S.R. Maidur, P.S. Patil, A. Ekbote, T.S. Chia, C.K. Quah, Molecular structure, second-and third-order nonlinear optical properties and DFT studies of a novel non-centrosymmetric chalcone derivative:(2E)-3-(4-fluorophenyl)-1-(4-{[(1E)-(4-fluorophenyl) methylene] amino} phenyl) prop-2-en-1-one, Spectrochim. Acta Mol. Biomol. Spectrosc. 184 (2017) 342–354.
[103] A. Arunkumar, P. Ramasamy, Bulk single crystals of ammonium acid phthalate grown by the Sankaranarayanan–Ramasamy method for optical limiting applications, J. Cryst. Growth 401 (2014) 195–199.
[104] M. Vinolia, S.S. Kirupavathy, S. Muthu, Synthesis, growth, structure, experimental and theoretical characterization on a novel second-order nonlinear optical single crystal: piperidin-1-ium 2-chloro-4-nitrobenzoate (P2CNB), J. Mater. Sci. Mater. Electron. 34 (9) (2023) 838.
[105] P. Karuppasamy, T. Kamalesh, K. Anitha, S.A. Kalam, M.S. Pandian, P. Ramasamy, S. Verma, S.V. Rao, Synthesis, crystal growth, structure and characterization of a novel third order nonlinear optical organic single crystal: 2-amino 4, 6-dimethyl pyrimidine 4-nitrophenol, Opt. Mater. 84 (2018) 475–489.
[106] A. Swamynayaka, M.S. Srinivas, V. Vahini, H.A. Khamees, M. Madegowda, V. N. Hegde, T.A. Hegde, G. Vinitha, Third-order nonlinear optical studies of Bis (4-methylbenzylammonium) tetrachloridocuprate metal-organic crystal with optical limiting behavior: experimental and theoretical investigations, J. Mol. Struct. 1269 (2022) 133827.
[107] D. Shalini, P. Vinothkumar, K. Sathyamoorthy, P. Muralimanohar, T.A. Hegde, G. Vinitha, M. Mohapatra, P. Murugasen, Synthesis, crystal structure and solid-state properties of 4-(3-nitrophenylamino)-4-methylpentan-2-one picrate (3NAP): an efficient cocrystal for χ (3) optics, J. Mol. Struct. 1225 (2021) 129098.
[108] K. Hatua, P.K. Nandi, Static second hyperpolarizability of Λ shaped alkaline earth metal complexes, J. Theor. Comput. Chem. 13 (5) (2014) 1450039.
[109] H. Abbas, M. Shkir, S. AlFaify, Density functional study of spectroscopy, electronic structure, linear and nonlinear optical properties of l-proline lithium chloride and l-proline lithium bromide monohydrate: for laser applications, Arab. J. Chem. 12 (8) (2019) 2336–2346.
[110] M. Shkir, S. AlFaify, M. Arora, V. Ganesh, H. Abbas, I. Yahia, A first principles study of key electronic, optical, second and third order nonlinear optical properties of 3-(4-chlorophenyl)-1-(pyridin-3-yl) prop-2-en-1-one: a novel D-π-A type chalcone derivative, J. Comput. Electron. 17 (1) (2018) 9–20.
[111] K. Govindarasu, E. Kavitha, Molecular structure, vibrational spectra, NBO, UV and first order hyperpolarizability, analysis of 4-Chloro-dl-phenylalanine by density functional theory, Spectrochim. Acta Mol. Biomol. Spectrosc. 133 (2014) 799–810.